

The Steep-spectrum Radio-loud AGN Luminosity Function and Its Implications for Black Hole Growth and Star Formation

WENJIE WANG,^{1,2,3} ZUNLI YUAN,^{1,2,3} B. ŠLAUS,^{4,5} HONGWEI YU,^{1,2,3} AND YU LUO^{1,2,3}

¹*Department of Physics, School of Physics and Electronics, Hunan Normal University, Changsha 410081, China*

²*Key Laboratory of Low Dimensional Quantum Structures and Quantum Control, Hunan Normal University, Changsha 410081, China*

³*Human Research Center of the Basic Discipline for Quantum Effects and Quantum Technologies, Hunan Normal University, Changsha 410081, China*

⁴*Department of Physics, Faculty of Science, University of Zagreb, Bijenička cesta 32, 10000 Zagreb, Croatia*

⁵*Astronomical Observatory Institute, Faculty of Physics and Astronomy, Adam Mickiewicz University, ul. Słoneczna 36, 60-286, Poznań, Poland*

ABSTRACT

We study the cosmic evolution of radio-loud active galactic nuclei (AGNs) using a beaming-minimized sample of 4,555 steep-spectrum sources over $0 < z \lesssim 4$, compiled from the XXL survey, VLA-COSMOS, and other wide-field data sets. We model the rest-frame 1.4 GHz radio luminosity function (RLF) with a luminosity-and-density evolution (LADE; DE+LE) framework coupled to a flexible local LF family. Among the tested parameterizations, Model C is statistically preferred and provides a globally consistent description of the binned RLFs while remaining compatible with local RLF measurements and Euclidean-normalized source counts. In the fiducial solution, the LE term rises toward cosmic noon ($z \sim 2-3$) and then flattens or mildly declines, whereas the DE term decreases monotonically with redshift. This combined evolution naturally reproduces the observed luminosity-dependent turnover redshift $z_{\text{peak}}(L)$ (often termed “cosmic downsizing”) without imposing *a priori* distinct evolutionary laws for low- and high-power sources. We further show that the same LADE functional family calibrated for star-forming galaxies also describes radio-loud AGNs when fitted independently, enabling a unified two-component (SFG+AGN) model consistent with both the local RLF and source-count statistics. Finally, converting the AGN RLF to a kinetic luminosity function yields a radio-mode black hole accretion rate density (BHAD) whose redshift dependence closely tracks the radio-based cosmic star formation rate density (after a conventional rescaling), with both histories peaking near $z \sim 2$.

Keywords: Galaxy evolution(594); Luminosity function(942); Radio continuum emission(1340); Active galaxies(17)

1. INTRODUCTION

Radio-loud active galactic nuclei (AGNs) inject mechanical energy through relativistic jets and are widely regarded as a key channel of AGN feedback in galaxy evolution (Heckman & Best 2014). Empirically, the link between supermassive black hole (SMBH) growth and galaxy evolution is supported by both indirect scaling relations between SMBH mass and host-galaxy properties (Magorrian et al. 1998; Ferrarese & Merritt 2000; Gebhardt et al. 2000; Graham et al. 2011; Sani et al. 2011; Beifiori et al. 2012; McConnell & Ma 2013) and direct feedback signatures such as powerful winds (e.g., Nesvadba et al. 2008; Feruglio et al. 2010; Veilleux et al. 2013; Tombesi et al. 2015) and X-ray cavities (Clarke et al. 1997; Rafferty et al. 2006; McNamara & Nulsen 2007; Fabian 2012; Nawaz et al. 2014; Kolokythas et al. 2015). Incorporating such feedback is now a cornerstone of modern galaxy-formation models (Bower et al. 2006; Croton et al. 2006; Schaye et al. 2015; Croton et al. 2016; Kaviraj et al. 2017; Springel et al. 2018; Davé et al. 2019).

Corresponding author: Zunli Yuan
yzl@hunnu.edu.cn

Corresponding author: Hongwei Yu
hwyu@hunnu.edu.cn

Quantifying the cosmic evolution of radio-loud AGNs is therefore essential for assessing the redshift dependence of jet-driven mechanical feedback and its contribution to SMBH growth.

A central statistical descriptor of the radio-loud AGN population is the radio luminosity function (RLF), which encodes the comoving space density as a function of radio luminosity and redshift (e.g., Smolčić et al. 2009; Rigby et al. 2015; Pracy et al. 2016; Novak et al. 2018). Combined with radio-kinetic scalings, the evolving RLF can be used to infer the cosmic history of jet kinetic output and SMBH growth in the kinetic (jet) mode (e.g., Kondapally et al. 2023; Smolčić et al. 2017a; Ceraj et al. 2018; Tucci & Toffolatti 2021). Observationally, RLF measurements have established that luminous radio-loud AGNs evolve strongly and peak around $z \sim 2-3$, whereas lower-luminosity sources evolve more mildly and peak at lower redshift, producing the luminosity-dependent peak redshift $z_{\text{peak}}(L)$, consistent with the commonly discussed “cosmic downsizing” phenomenology (e.g., Waddington et al. 2001; Clewley & Jarvis 2004; Rigby et al. 2011, 2015; Pracy et al. 2016).

Recent progress on this luminosity-dependent evolution RLF has been enabled by increasingly large, multi-field radio-loud AGN compilations. In particular, Šlaus et al. (2024) assembled one of the largest samples to date and showed that an luminosity-dependent density evolution (LDDE; Schmidt & Green 1983; Ueda et al. 2003) parameterization provides a satisfactory description of their data. However, their compilation includes a non-negligible fraction of flat-spectrum radio sources. These are preferentially jet-aligned systems, where Doppler boosting makes the compact jet core dominate over the optically-thin lobe emission, yielding an observed flat spectrum and a boosted apparent radio luminosity that can bias the inferred high-luminosity evolution (Urry & Padovani 1995; D’Ammando et al. 2019; Tucci & Toffolatti 2021). A more robust route to the intrinsic RLF evolution is therefore to exclude flat-spectrum sources and focus on steep-spectrum objects that are less susceptible to Doppler boosting.

Beyond LDDE, an alternative phenomenological description is the luminosity-and-density evolution (LADE) framework (e.g., Condon 1984; Aird et al. 2010; Yuan et al. 2016a), which models the RLF evolution as the combined action of a luminosity-evolution (LE) term and a density-evolution (DE) term (e.g., Yuan et al. 2016a; Yuan et al. 2017). In this decomposition, LE captures redshift-dependent shifts in the characteristic luminosity scale, while DE describes changes in the overall comoving abundance. Importantly, the observed luminosity-dependent peak redshift can emerge naturally from the joint DE+LE evolution acting on an LF whose slope varies with luminosity, without imposing *a priori* different evolutionary laws for low- and high-power sources. This makes LADE particularly well suited for interpreting the intrinsic evolution of steep-spectrum radio-loud AGNs (e.g., Yuan et al. 2017) once Doppler-boosted flat-spectrum objects are excluded. Notably, LADE has also been shown to provide a compelling description of the RLF of star-forming galaxies (SFGs) (Wang et al. 2024, 2026), enabling like-for-like AGN–SFG comparisons within the same functional architecture.

In this work, we adopt the multi-survey parent sample compiled by Šlaus et al. (2024) and refine it into a beaming-minimized steep-spectrum subsample by excluding flat-spectrum sources. We then model the rest-frame 1.4 GHz RLF within a LADE framework using a trivariate (L, z, α) RLF estimator that explicitly incorporates the spectral-index distribution. Finally, we convert the RLF to a kinetic luminosity function to infer the radio-mode black hole accretion rate density (BHAD) and compare its redshift dependence with the cosmic star formation rate density (SFRD).

This paper is organized as follows. Section 2 describes the multi-survey datasets and the steep-spectrum sample construction, including the exclusion of flat-spectrum radio sources. Section 3 presents the binned and parametric methodology, completeness treatment, the LADE model families and model selection, and the joint constraints from local RLFs and source counts. Section 4 presents the best-fit RLFs and evolutionary trends, including the inferred $z_{\text{peak}}(L)$. Section 5.2 derives BHAD and compares it with SFRD, and Section 6 summarizes our conclusions. Throughout this work, we assume a flat Λ cold dark matter (Λ CDM) cosmology with $H_0 = 70 \text{ km s}^{-1} \text{ Mpc}^{-1}$, $\Omega_\Lambda = 0.7$, and $\Omega_m = 0.3$. We adopt a power-law radio spectrum $F_\nu \propto \nu^{-\alpha}$, with the spectral index fixed to $\alpha = 0.7$ where required.

2. DATA AND SAMPLE SELECTION

2.1. Parent Sample

The radio AGN sample utilized in this work is based on the comprehensive catalog compiled by Šlaus et al. (2024), which originates from the XXL Survey Large Program. The data analysis and multi-band association procedure are fully described in that work, and we refer readers to that publication for a complete description. Here we summarize some key points about the sample.

This catalog incorporates data from a set of radio surveys with varying areas and depth. The XXL Survey provides intermediate-depth coverage from both the XXL-North and XXL-South fields, observed with the Giant Metrewave

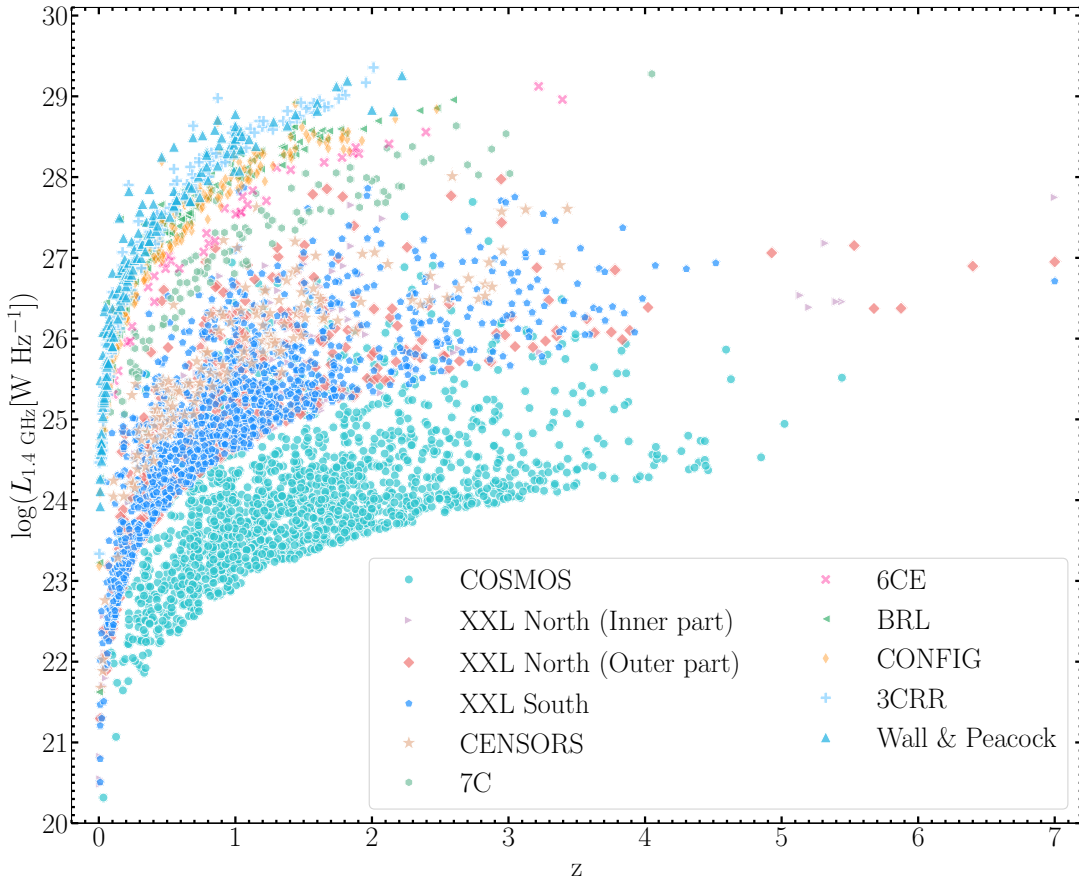


Figure 1. Redshift–luminosity distribution of the steep-spectrum radio-loud AGN sample used throughout this work (after excluding FSRQ sources)

. The corresponding survey fields are indicated in the legend.

Table 1. AGN data and FSRQ statistics across different surveys.

Survey	Original Number	FSRQ Number	Final Number	FSRQ fraction (%)
7C	128	27	101	21.09
6CE	58	21	37	36.21
3CRR	170	26	144	15.29
XXL-North (Inner)	292	86	206	29.45
XXL-North (Outer)	607	150	457	24.71
XXL-South	1484	279	1205	18.80
COSMOS	1916	170	1746	8.87
CENSORS	149	0	149	0.00
BRL	178	11	167	6.18
Wall & Peacock	227	64	163	28.19
Config	243	63	180	25.93

Radio Telescope (GMRT) at 610 MHz and the Australia Telescope Compact Array (ATCA) at 2.1 GHz, respectively (Smolčić et al. 2018; Butler et al. 2018). To capture both low- and high-luminosity AGN across a wide redshift range, the catalog includes additional wide and shallow surveys—3CRR, 6CE, and 7C—at 151 MHz (Willott et al. 2001), as well as deep-field observations from the VLA-COSMOS 3 GHz Large Project (Smolčić et al. 2017). Further contributions come from the Combined EIS–NVSS Survey of Radio Sources (CENSORS) at 1.4 GHz (Brookes et al.

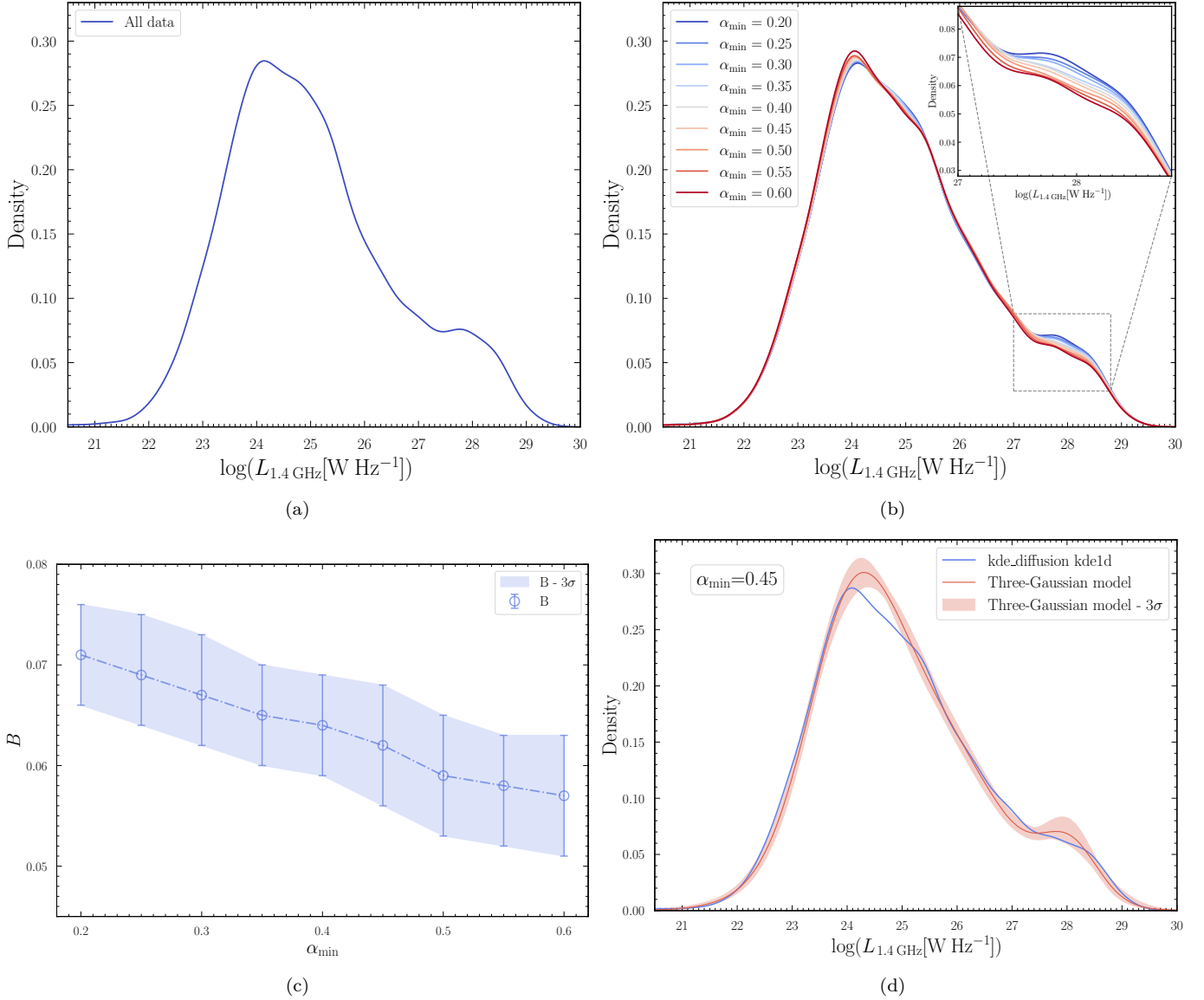


Figure 2. Panel (a): Kernel density estimate of the rest-frame 1.4 GHz luminosity distribution for the full AGN sample, highlighting the presence of three distinct components. Panel (b): Evolution of the height of the high-luminosity peak as a function of the minimum spectral index threshold α_{\min} , obtained by progressively removing sources with $\alpha < \alpha_{\min}$. Panel (c): Best-fitting weight B of the FSRQ component in the Three-Gaussian model (Equation 1) as a function of α_{\min} , with 3σ uncertainties. Panel (d): Comparison between the KDE result from KDE-diffusion and our Three-Gaussian model at $\alpha_{\min} = 0.45$; the two distributions agree within the uncertainties.

2008); the Best, Röttgering, and Lehnert (BRL) sample at 408 MHz (Best et al. 1999, 2000, 2003); the Wall & Peacock (1985) sample at 2.7 GHz; and the Combined NVSS–FIRST Galaxies (CoNFIG) sample at 1.4 GHz (Gendre & Wall 2008), many of which include a high fraction of spectroscopic redshifts. To ensure consistency across surveys with different observing frequencies, all fluxes were converted to 1.4 GHz using a power-law spectrum and survey-specific spectral indices or their mean values (see Šlaus et al. 2024, Table 1).

To construct a clean AGN sample, additional selection criteria were applied based on survey characteristics. For the XXL-North and XXL-South fields, sources with flux densities above 1 mJy were retained to minimize contamination from SFGs. In the COSMOS field, AGN were selected based on a radio-excess criterion relative to infrared-based star formation rates. Bright-flux surveys (e.g., 3CRR, 6CE) required no additional cuts.

The final sample consists of 5,452 AGN spanning the redshift range $0 < z \lesssim 7$ and radio luminosities in the range $20 \lesssim \log(L_{1.4\text{GHz}}) \lesssim 29.5$. A redshift–luminosity diagram of the sample is presented in Figure 1, illustrating the ranges in redshift and luminosity that each survey spans. We also present in Figure 2(a) the distribution of the rest-frame 1.4 GHz luminosity, $\log L_{1.4\text{GHz}}$, derived using the diffusion-based kernel density estimation (KDE) method of Botev et al. (2010), as implemented in the Python package `KDE-diffusion`¹. The AGN sample can be decomposed into three primary components: low-luminosity AGNs, high-luminosity AGNs, and flat-spectrum radio quasars (FSRQs). The latter population has been excluded from the analysis. A detailed explanation is provided below.

2.2. Exclusion of Flat-Spectrum Radio Quasars

Flat-spectrum sources are typically defined as those with a spectral index $\alpha < 0.5$, while steep-spectrum sources have $\alpha > 0.5$. Since the relativistic jets of FSRQs are oriented at small angles to our line of sight, Doppler boosting significantly enhances their observed luminosities relative to their intrinsic values. Consequently, their apparent luminosity distribution is strongly affected by orientation and selection effects, rather than reflecting the intrinsic population evolution of radio AGNs. For this reason, FSRQs are excluded from our analysis of the RLF.

As shown in Figure 2(a), the luminosity distribution clearly exhibits a prominent tri-modal structure. Accordingly, we model it using a Three-Gaussian mixture

$$\begin{aligned}
 f(x) = & (1 - A - B) \cdot \frac{1}{\sqrt{2\pi}\sigma_1} \exp\left(-\frac{(x - \mu_1)^2}{2\sigma_1^2}\right) \\
 & + A \cdot \frac{1}{\sqrt{2\pi}\sigma_2} \exp\left(-\frac{(x - \mu_2)^2}{2\sigma_2^2}\right) \\
 & + B \cdot \frac{1}{\sqrt{2\pi}\sigma_3} \exp\left(-\frac{(x - \mu_3)^2}{2\sigma_3^2}\right),
 \end{aligned} \tag{1}$$

and employ the Markov Chain Monte Carlo (MCMC) method to infer the best-fitting parameters along with their associated uncertainties, where $x \equiv \log L_{1.4\text{GHz}}$. We applied the Three-Gaussian model to the entire AGN sample. Using the MCMC method, we obtained the best-fit peak positions of the three components as $\mu_1 = 24.04$, $\mu_2 = 25.139$, and $\mu_3 = 28.053$. In the subsequent analysis, these values are held fixed, under the assumption that the peak locations of the three components remain invariant.

As shown in Figure 2(b), by gradually increasing the lower limit on the spectral index α_{min} (ranging from 0.2 to 0.6) and removing sources with $\alpha < \alpha_{\text{min}}$, the height of the third peak decreases systematically. This indicates that the number of FSRQs declines with increasing spectral index threshold.

We then applied the Three-Gaussian model described in Equation 1 at each value of α_{min} and performed MCMC fitting to obtain the corresponding weight B of the FSRQ component together with its associated 3σ uncertainty. As illustrated in Figure 2(c), this weight also decreases with increasing α_{min} , exhibiting a consistent trend.

Based on these results, we adopt $\alpha_{\text{min}} = 0.45$ as the final selection criterion to identify FSRQs. The choice of $\alpha_{\text{min}} = 0.45$ represents a balance between completeness and purity. A higher threshold would remove more FSRQs but might also exclude some genuine steep-spectrum AGNs, while a lower threshold would retain more sources but may fail to fully eliminate the FSRQ contamination. After excluding the FSRQ component, the final sample consists of 4,555 sources. The FSRQ statistics across the individual surveys are summarized in Table 1. This refined dataset constitutes the steep-spectrum AGN sample utilized for the luminosity function analysis throughout the rest of this paper. Figure 2(d) compares the KDE result obtained with the diffusion-based estimator of Botev et al. (2010) (via the `KDE-diffusion` package) with our Three-Gaussian model at $\alpha_{\text{min}} = 0.45$. The two distributions agree within the uncertainties.

Based on these results, we adopt $\alpha_{\text{min}} = 0.45$ as the final selection criterion to identify FSRQs. The choice of $\alpha_{\text{min}} = 0.45$ represents a balance between completeness and purity. A higher threshold would remove more FSRQs but might also exclude some genuine steep-spectrum AGNs due to spectral-index uncertainties, variability/non-simultaneous multi-frequency measurements, and spectral curvature, while a lower threshold would retain more sources but may fail to fully eliminate the FSRQ contamination. We note that flat-spectrum sources are not necessarily all strongly Doppler-boosted on an object-by-object basis, but they are statistically more susceptible to beaming-related luminosity

¹ <https://pypi.org/project/KDE-diffusion/>

inflation, motivating their removal to mitigate bias in the LF analysis. After excluding the FSRQ component, the final sample consists of 4,555 sources. The FSRQ statistics across the individual surveys are summarized in Table 1. This refined dataset constitutes the steep-spectrum AGN sample utilized for the luminosity function analysis throughout the rest of this paper. Figure 2(d) compares the KDE result obtained with the diffusion-based estimator of Botev et al. (2010) (via the KDE-diffusion package) with our Three-Gaussian model at $\alpha_{\min} = 0.45$. The two distributions agree within the uncertainties.

3. METHODS

In this work, the AGN LF is estimated using both binned and parametric methods, which are briefly summarized below.

3.1. The binned estimator

To estimate the binned LF of AGNs, we adopt the method proposed by Page & Carrera (2000) (hereafter referred to as the PC method), which can be viewed as a statistically refined version of the classical $1/V_{\max}$ approach (Schmidt 1968). Unlike the $1/V_{\max}$ method, which assigns each object an individual weight based on its maximum accessible volume, the PC method computes the LF by integrating over the *actual surveyed region* of each luminosity–redshift (L – z) bin.

For a given luminosity and redshift bin defined by $[L_1, L_2]$ and $[z_1, z_2]$, the LF at the center of the bin, as estimated by the PC method, is given by

$$\phi_{\text{PC}} = \frac{N}{\int_{L_1}^{L_2} \int_{z_1}^{z_{\max}(L)} \frac{dV}{dz} dz dL}, \quad (2)$$

where N is the number of AGNs observed in the bin, and the denominator reflects the volume actually accessible within the bin, constrained by the survey flux limit.

3.2. The parametric method

The estimation of the AGN RLF can be significantly affected by the spectral index distribution of the sources (see Jarvis & Rawlings 2000; Jarvis et al. 2001; Yuan et al. 2016a). As pointed out by Yuan et al. (2016a), neglecting this effect may lead to biased results, especially for flat-spectrum sources whose spectral indices exhibit large scatter. They demonstrated through Monte Carlo simulations that traditional bivariate estimators often fail to properly account for the complex truncation boundaries on the L – z plane introduced by K -corrections. To address this issue, Yuan et al. (2016a) proposed incorporating the spectral index distribution directly into the RLF analysis by introducing a trivariate function $\Phi(\alpha, z, L)$, which provides a more accurate and robust framework for estimating the RLF of AGNs. Motivated by their work, we adopt a similar parametric approach that explicitly takes into account the spectral index distribution when modeling the AGN RLF.

3.2.1. The trivariate RLF

Following Yuan et al. (2017), we define the trivariate RLF as the number density of sources per unit comoving volume dV per unit logarithmic luminosity interval $d \log L$, and per unit spectral index interval $d\alpha$

$$\Phi(\alpha, z, L) = \frac{d^3 N}{d\alpha dV d \log L}. \quad (3)$$

If the spectral index distribution, $dN/d\alpha$, is independent of redshift and luminosity, the trivariate RLF can be factorized as the product of the conventional (bivariate) RLF, $\phi(z, L)$, and the intrinsic spectral index distribution:

$$\Phi(\alpha, z, L) = \phi(z, L) \times \frac{dN}{d\alpha}. \quad (4)$$

Given an analytical form of the LF parameterized by θ , denoted as $\Phi(\alpha, z, L | \theta)$, the optimal parameter set θ is obtained by minimizing the negative log-likelihood function S . Following Yuan et al. (2017), and adopting the general treatment of completeness corrections in Marshall et al. (1983) and Fan et al. (2001), the likelihood function S for a

single survey field can be written in the unified form

$$S_{\text{single}} = -2 \sum_{i=1}^n \ln [\Phi(\alpha_i, z_i, L_i) p(z_i, L_i)] + 2 \iiint_W \Phi(\alpha, z, L) p(z, L) \Omega \frac{dV}{dz} dz dL d\alpha, \quad (5)$$

where Ω is the solid angle of the survey, W denotes the survey region in the (α, z, L) space, and $p(z, L)$ is the completeness correction factor as a function of redshift and luminosity. In this formalism, a completely sampled field is treated as the special case with $p(z, L) \equiv 1$.

Among our eleven survey fields, data from eight fields (7C, 6CE, 3CRR, XXL-South, CENSORS, BRL, Wall & Peacock, and Config) are considered to be complete, and we therefore set $p(z, L) \equiv 1$ for these fields. The remaining three fields—XXL-North (Inner), XXL-North (Outer), and COSMOS—are classified as incomplete. For the XXL-North field, the completeness factor $p(z, L)$ incorporates two principal components: one accounting for detection-limit noise (Smolčić et al. 2018), and another addressing redshift-dependent matching losses (Šlaus et al. 2020). For the COSMOS field, the corresponding completeness correction is adopted from Smolčić et al. (2017b), specifically their Figure 16 and Table 2. We compute $p(z, L)$ following the same procedure as described in Wang et al. (2024).

This unified expression can be naturally generalized to the case of multiple survey fields indexed by j , each characterized by its own LF Φ_j , completeness function $p_j(z, L)$, survey region W_j , and solid angle Ω_j . The total likelihood function S_{all} that incorporates all fields is then

$$S_{\text{all}} = -2 \sum_j \sum_{i=1}^{n_j} \ln [\Phi_j(\alpha_i, z_i, L_i) p_j(z_i, L_i)] + 2 \sum_j \iiint_{W_j} \Phi_j(\alpha, z, L) p_j(z, L) \Omega_j \frac{dV}{dz} dz dL d\alpha, \quad (6)$$

where n_j is the number of sources in field j , and thus $n = \sum_j n_j$ is the total number of sources. In this notation, fields with complete data correspond to $p_j(z, L) \equiv 1$, while incomplete fields adopt the non-trivial completeness functions $p_j(z, L)$ described above.

To further constrain the model, we adopt the approach of Willott et al. (2001) and Yuan et al. (2017) by incorporating recent measurements of the local radio LF (LRLF) and SCs into the fitting procedure. Since both LRLF and SC are one-dimensional distributions, their influence on the fitting is quantified via the standard χ^2 statistic

$$\chi^2 = \sum_{i=1}^n \left(\frac{f_{\text{data } i} - f_{\text{mod } i}}{\sigma_{\text{data } i}} \right)^2, \quad (7)$$

where $f_{\text{data } i}$ is the observed value in the i th bin, while $f_{\text{mod } i}$ and $\sigma_{\text{data } i}$ are the corresponding model prediction and observed error, respectively. Since χ^2 is related to the likelihood via $\chi^2 = -2 \ln(\text{likelihood})$ (i.e., the same form as S ; Willott et al. 2001), we define a combined likelihood function S_{joint} that incorporates constraints from all three components of data (AGN data, LRLF data, and SC data). The expression is

$$S_{\text{joint}} = S_{\text{all}} + \chi_{\text{LRLF}}^2 + \chi_{\text{SC}}^2, \quad (8)$$

where χ_{LRLF}^2 and χ_{SC}^2 denote the value of χ^2 for the local radio LFs and SCs, respectively. Using Equation (8), the best-fit parameters of the LF are obtained by numerically minimizing the objective function S_{joint} . Following the Bayesian framework adopted in our previous work (e.g., Yuan et al. 2016a), we estimate both the optimal parameter values and their posterior distributions (see also Yuan et al. 2017). We assume uniform (i.e., uninformative) priors for all parameters and perform MCMC sampling using the EMCEE Python package (Foreman-Mackey et al. 2013).

3.3. Constraints from Local LFs and Source Counts

The local LFs at 1.4 GHz have been well determined for AGNs through the combination of large radio surveys, such as NVSS (NRAO VLA Sky Survey) and FIRST (Faint Images of the Radio Sky at Twenty centimeters), with wide-area spectroscopic surveys. In this work, we jointly adopt the local AGN LFs reported by Condon et al. (2002),

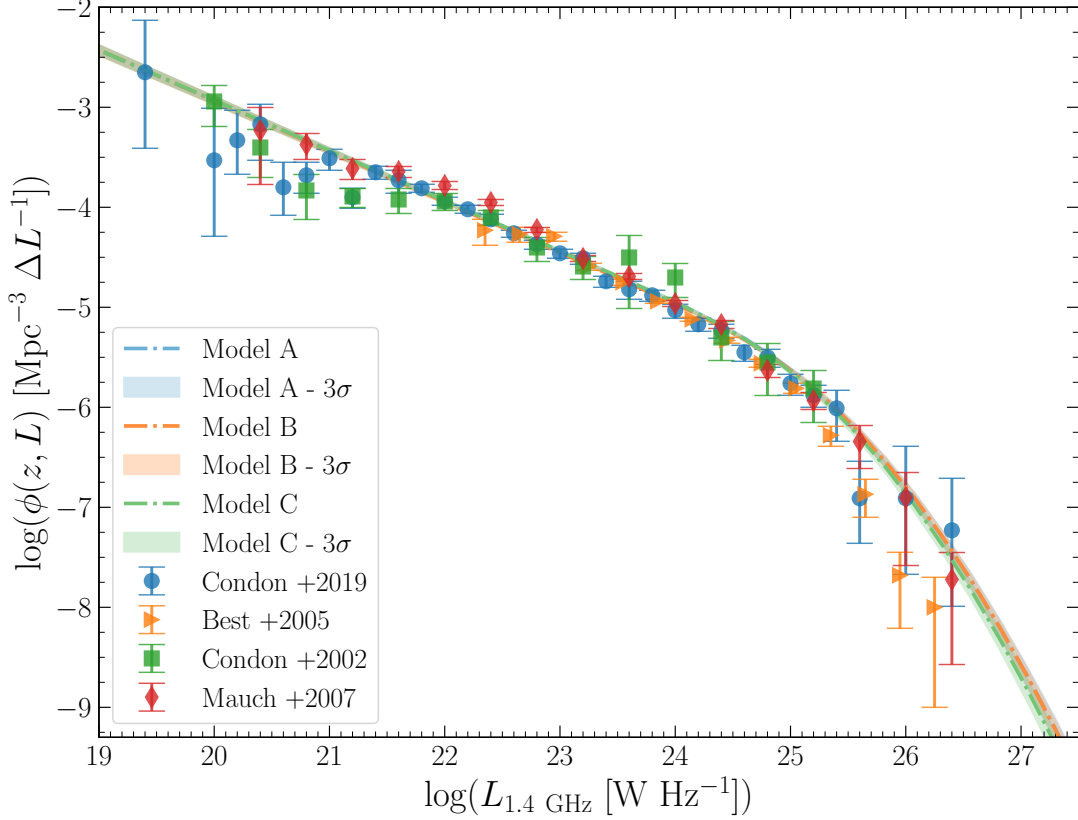


Figure 3. Local radio LF at 1.4 GHz of AGN from several surveys with different observed areas and sensitivities (colored data points). The colored lines show the fits to the combined data from our models.

Best et al. (2005), Mauch & Sadler (2007), and Condon et al. (2019) (see Figure 3) to calculate χ^2_{LRLF} in Equation (8), by summing the χ^2 contributions from the individual literature local-LF datasets.

In addition to the local LFs, radio SCs provide important constraints for modeling the AGN LFs. The differential SCs, denoted as $n(F_\nu)$, describe the number of sources per unit flux density F_ν per steradian. Their distribution reflects both the cosmic evolution of the sources and the geometry of the Universe (Padovani 2016). The SCs are typically normalized to a Euclidean slope by multiplying by $F_\nu^{2.5}$ (e.g., de Zotti et al. 2010). Following Yuan et al. (2017), the AGN SCs can be related to their LF via

$$\frac{n(F_\nu)}{4\pi} = 4\pi \frac{c}{H_0} \times \int_{z_1}^{z_2} \int_{\alpha_1}^{\alpha_2} \frac{\Phi(\alpha, z, L(\alpha, z, F_\nu)) D_L^4(z) d\alpha dz}{(1+z)^{(3-\alpha)} \sqrt{\Omega_M(1+z)^3 + \Omega_\Lambda}}, \quad (9)$$

where c is the speed of light, $\Phi(\alpha, z, L)$ is the LF, $D_L(z)$ is the luminosity distance, z_1 and z_2 , α_1 and α_2 represent the integration limits of redshift and spectral index (Padovani 2016).

To further constrain our RLF model, we incorporate observed AGN radio SCs from de Zotti et al. (2010), Padovani et al. (2015), Smolčić et al. (2017b), Algera et al. (2020), and Hale et al. (2023). These datasets collectively span a wide range in frequency, flux density, and survey area, thereby providing complementary constraints on both the faint and bright ends of the AGN population. For consistency across all samples, SCs measured at frequencies other than 1.4 GHz are converted to their equivalent 1.4 GHz values assuming a power-law radio spectrum.

These datasets are chosen for their complementary strengths. The compilation by de Zotti et al. (2010) provides particularly broad coverage in flux density and frequency. From the E-CDFS VLA survey, Padovani et al. (2015) present a detailed decomposition of the sub-mJy radio population into radio-quiet (RQ) and radio-loud (RL) AGN based on extensive multiwavelength information, which we use to anchor the AGN contribution at intermediate flux densities. The VLA-COSMOS 3 GHz Large Project (Smolčić et al. 2017b) covers 2 deg^2 and reaches a 5σ detection threshold of $\sim 11.5 \mu\text{Jy}$; we adopt the AGN SCs derived from their multiwavelength classification scheme to further constrain

the faint end. In addition, we utilize the AGN SCs from the ultra-deep Karl G. Jansky VLA COSMOS-XS survey of [Algera et al. \(2020\)](#), which reaches an rms sensitivity of $\sim 0.53 \mu\text{Jy beam}^{-1}$ at 3 GHz over an area of $\sim 350 \text{ arcmin}^2$. In that work, AGN are identified via multiwavelength diagnostics and subdivided into moderate-luminosity AGN (MLAGN) and high-luminosity AGN (HLAGN) according to their dominant emission mechanisms. Finally, [Hale et al. \(2023\)](#) present AGN SCs based on the 1.4 GHz continuum Early Science data release of the MeerKAT MIGHTEE survey, which covers $\sim 5 \text{ deg}^2$ across the COSMOS and XMM-LSS fields; AGN are identified using multiwavelength diagnostics, and the SCs are corrected for incompleteness via extensive simulations.

A critical aspect of using the MIGHTEE counts from [Hale et al. \(2023\)](#) is the treatment of sources without secure classifications (“unmatched” sources). They consider two schemes: (1) a flux-dependent probabilistic split between SFGs and AGN, based on the fractions observed in the classified sample within each flux bin, and (2) the extreme assumption that all unmatched sources are SFGs. In this work, we adopt the first, physically motivated approach, which assumes that the relative AGN fraction among unmatched sources mirrors that of the classified population in each flux bin. Accordingly, for both the COSMOS and XMM-LSS fields, we use the AGN SCs tabulated in the $SC_{\text{AGN, ratio}}$ column of Tables 1 and 2 in [Hale et al. \(2023\)](#).

3.4. Models for the AGN LFs

Following [Yuan et al. \(2017\)](#), the trivariate RLF can be defined as

$$\Phi(\alpha, z, L) = e_1(z)\phi(z = 0, L/e_2(z), \eta^j) \frac{dN}{d\alpha}, \quad (10)$$

where $e_1(z)$ and $e_2(z)$ represent DE and LE with redshift, respectively, and η^j denote the parameters that characterize the shape of the radio LF. If η^j remains invariant across redshift, this suggests that the intrinsic shape of the radio LF is preserved. In contrast, a redshift-dependent η^j implies luminosity-dependent density evolution (for a more detailed discussion, see [Singal et al. 2013, 2014](#)). In this work, we adopt the commonly used assumption that the LF shape does not vary with redshift (i.e., η^j is fixed), consistent with several previous studies (e.g., [Yuan et al. 2017](#); [Novak et al. 2017](#); [van der Vlugt et al. 2022](#); [Wang et al. 2024](#)).

In this work, the local AGN LF $\phi(z = 0, L/e_2(z = 0))$ is modeled using the modified Schechter function proposed by [Saunders et al. \(1990\)](#):

$$\phi(z = 0, L/e_2(z = 0)) = \frac{dN}{d \log L} = \phi_* \left(\frac{L}{L_*} \right)^{1-\beta} \exp \left[-\frac{1}{2\gamma^2} \log^2 \left(1 + \frac{L}{L_*} \right) \right], \quad (11)$$

where L_* marks the knee of the LF, β and γ control the slopes at the faint and bright ends, respectively, and ϕ_* is the normalization factor of $\phi(z, L)$. This functional form is commonly used to describe the local LF of SFGs (e.g., [Novak et al. 2017](#); [Ocran et al. 2020](#); [Enia et al. 2022](#); [van der Vlugt et al. 2022](#); [Cochrane et al. 2023](#); [Wang et al. 2024](#)). More recently, it has also been adopted to model the local LF of AGNs (e.g., [Šlaus et al. 2024](#)). In our analysis, we find that this form provides a better fit compared to other traditional prescriptions for AGN local LFs, such as the double power-law model (e.g., [Boyle et al. 2000](#); [Ajello et al. 2012](#); [Yuan et al. 2016a](#)) or the alternative modified Schechter function (e.g., [Pei 1995](#); [Hopkins et al. 2007](#); [Yuan et al. 2017](#)).

In this work, we investigate three distinct evolutionary scenarios, designated as Model A, Model B, and Model C. Models A and B share an identical DE function, $e_1(z)$, parameterized as a simple exponential decay:

$$e_1(z) = e^{-p_1 z}. \quad (12)$$

The models are differentiated by their LE functions. For Model A, we adopt a standard power-law evolution:

$$e_2(z) = (1 + z)^{k_1}. \quad (13)$$

In Model B, to prevent the LE from increasing indefinitely with redshift, we introduce a redshift-dependent power-law index:

$$e_2(z) = (1 + z)^{k_1 + k_2 z}. \quad (14)$$

Finally, Model C represents our most flexible scenario. It allows for a more complex density evolution structure than the simple monotonic decline assumed in Models A and B. Model C retains the LE function of Model B but adopts a

Table 2. Model comparison based on information criteria. The left panel shows the AIC and BIC statistics for the full sample, while the right panel presents the AIC statistics for the restricted subset ($0 < z < 3.5$) to test the robustness of the models against high-redshift selection effects. Δ values are computed relative to Model C, which provides the minimum values in both cases.

Model	Full Sample				Subset ($0 < z < 3.5$)	
	AIC	Δ AIC	BIC	Δ BIC	AIC	Δ AIC
A	126913.9	44.2	126965.3	31.3	125255.3	49.1
B	126888.2	18.5	126946.0	12.0	125228.6	22.4
C	126869.7	0.0	126934.0	0.0	125206.2	0.0
LDDE	127580.5	710.8	127651.2	717.2	–	–

DE function mirroring the mathematical form of the LE:

$$e_1(z) = (1+z)^{p_1+p_2z}. \quad (15)$$

Notably, the functional forms of Model B and Model C are identical to those successfully applied to the SFG population in our previous work (Wang et al. 2024). These parameterizations fall under the general category of mixture evolution (e.g., Yuan et al. 2016a; Yuan et al. 2017) or LADE (e.g., Aird et al. 2010) models.

Regarding the intrinsic spectral index distribution, $dN/d\alpha$, Yuan et al. (2017) demonstrated that a right-skewed distribution offers a superior description for steep-spectrum sources. Following their approach, we adopt the log-normal form:

$$\frac{dN}{d\alpha} = \frac{1}{\sqrt{2\pi}\alpha\sigma} e^{-\frac{(\ln\alpha-\mu)^2}{2\sigma^2}} \quad (16)$$

3.5. Model selection

To quantitatively compare the performance of different models, we adopt model selection criteria based on information theory (Takeuchi 2000). One widely used metric is the Akaike Information Criterion (AIC; Akaike 1974), which balances model fit and complexity. It is defined as

$$\text{AIC} = S_{\text{all}}(\hat{\theta}) + 2q, \quad (17)$$

where $S_{\text{all}}(\hat{\theta})$ is the total likelihood statistic evaluated at the best-fit parameters $\hat{\theta}$, and q denotes the number of free parameters.

An alternative criterion is the Bayesian Information Criterion (BIC; Schwarz 1978), which introduces a stronger penalty for model complexity:

$$\text{BIC} = S_{\text{all}}(\hat{\theta}) + q \ln n, \quad (18)$$

where n is the effective sample size. For model comparison we use only the AGN LF likelihood, i.e. AIC and BIC are computed from S_{all} without including the χ^2 constraints from the LRLF and source counts.

4. RESULTS

In this section, we present the derived AGN radio LF, quantify their evolution across cosmic time, and compare the results from our LADE model with an alternative LDDE model. We also explore how our findings relate to existing work on the luminosity-dependent evolution of radio AGN and, finally, examine evidence for a coevolution between AGN and SFGs.

4.1. Best-fit Luminosity Functions

The parameters of our model LFs are constrained using the MCMC algorithm implemented via the EMCEE Python package (Foreman-Mackey et al. 2013). This ensemble sampler employs multiple chains initialized from different starting points, allowing for an efficient and robust exploration of the parameter space while avoiding local minima. We adopt uniform priors for all model parameters. The one- and two-dimensional marginalized posterior distributions for Models A, B, and C are presented in Figures 12–14, demonstrating that all parameters are well constrained. The best-fit values along with their corresponding 1σ uncertainties are summarized in Table 3.

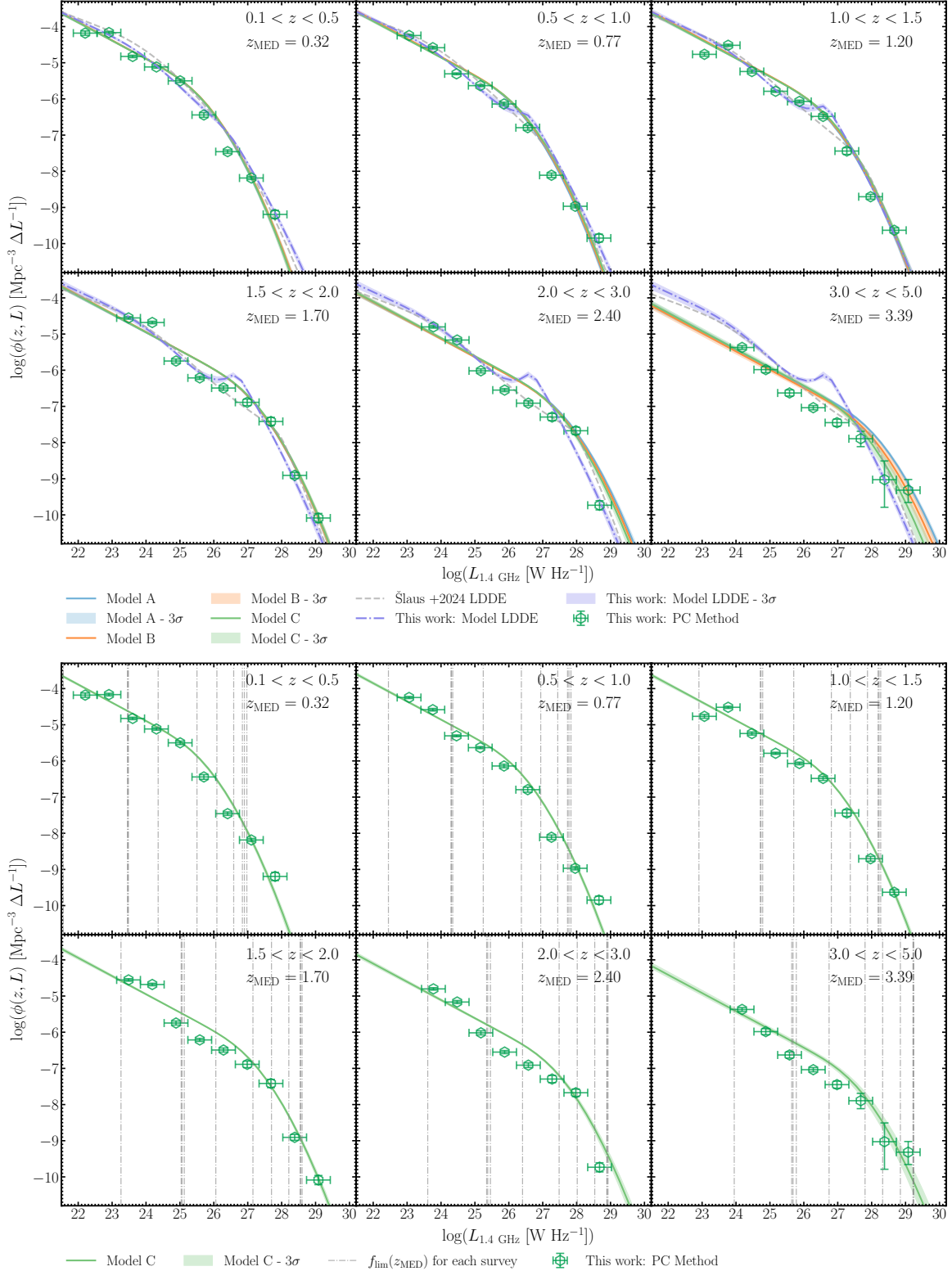


Figure 4. Radio LFs of AGNs in different redshift bins, compared with the nonparametric LFs obtained using the PC method (green open hexagons). The best-fitting parametric LFs for Models A, B, and C are shown as blue, orange, and green solid curves, respectively, with shaded bands indicating the corresponding 3σ confidence regions. For comparison, the grey dashed curves show the LDDE model of Šlaus et al. (2024), while the purple dash-dotted curves depict our LDDE-based fits, with their 3σ confidence intervals indicated by the purple shaded regions. The top panels display the full comparison among Models A, B, and C, whereas the bottom panels only show Model C and its 3σ confidence region together with the PC-based LFs, to highlight the agreement between our fiducial model and the nonparametric estimates. The vertical grey dash-dotted lines in the bottom panels mark the flux limits of the individual surveys contributing to each redshift bin.

Table 3. Best-fit parameters for models A, B, and C

Model	$\log_{10}(\phi_*)$	$\log_{10}(L_*)$	β	γ	k_1	k_2	p_1	p_2	μ	σ
A	$-5.043_{-0.023}^{+0.023}$	$24.115_{-0.038}^{+0.038}$	$1.503_{-0.004}^{+0.004}$	$0.862_{-0.009}^{+0.009}$	$4.661_{-0.072}^{+0.072}$...	$1.330_{-0.024}^{+0.024}$...	$-0.235_{-0.005}^{+0.005}$	$0.280_{-0.004}^{+0.004}$
B	$-5.080_{-0.026}^{+0.026}$	$24.147_{-0.041}^{+0.041}$	$1.507_{-0.004}^{+0.004}$	$0.853_{-0.010}^{+0.010}$	$4.915_{-0.090}^{+0.090}$	$-0.151_{-0.036}^{+0.036}$	$1.296_{-0.027}^{+0.027}$...	$-0.235_{-0.005}^{+0.005}$	$0.282_{-0.004}^{+0.004}$
C	$-4.985_{-0.031}^{+0.031}$	$24.024_{-0.049}^{+0.049}$	$1.503_{-0.004}^{+0.004}$	$0.848_{-0.011}^{+0.011}$	$6.010_{-0.180}^{+0.180}$	$-0.583_{-0.069}^{+0.069}$	$-2.220_{-0.120}^{+0.120}$	$-0.149_{-0.043}^{+0.043}$	$-0.236_{-0.005}^{+0.005}$	$0.282_{-0.004}^{+0.004}$

Note. Units — ϕ_* : [$\text{Mpc}^{-3} \text{ dex}^{-1}$], L_* : [W Hz^{-1}]. The best-fit parameters and their 1σ uncertainties are shown for models A, B, and C.

Figure 4 presents the best-fit RLFs derived from our Models A (blue), B (orange), and C (green solid lines), together with the binned estimates from the PC method (green open hexagons). In this plot, all RLFs are evaluated at the rest-frame frequency of 1.4 GHz. We also plot the original LDDE model from Šlaus et al. (2024) (grey dashed line). Since that model was derived from the broader parent sample containing FSRQs, it is not strictly comparable to our steep-spectrum results. To enable a rigorous comparison, we fitted the same LDDE functional form to our defined steep-spectrum sample, accounting for the intrinsic spectral index distribution. The resulting fit, referred to as our trivariate LDDE model (purple dash-dotted line), serves as a robust baseline for evaluating our LADE models.

Qualitatively, our three models are virtually indistinguishable across the entire luminosity range at $z \lesssim 2.5$. It is only at higher redshifts ($z \gtrsim 2.5$) that minor differences begin to emerge at the high-luminosity end. Moreover, our LADE-based models show good overall agreement with the PC-derived binned RLFs, reproducing the main trends within the uncertainties; however, we note that the binned data points lie systematically below the model curves in several luminosity bins. This behavior is expected and can be attributed to two primary methodological effects discussed below.

First, while it is common practice to regard binned estimates as ‘observed LFs’ and use them as a benchmark to validate parametric models, we must emphasize a critical caveat regarding our composite sample. Since our dataset combines 11 sub-surveys with distinct flux limits, the flux-limit curves of these different fields inevitably cross multiple luminosity bins within any given redshift interval. Consequently, the resulting binned LFs are highly sensitive to the choice of binning—a manifestation of boundary bias (e.g., Yuan & Wang 2013). While such bias is typically confined to the faintest bins in a single-flux-limit sample, the multiple thresholds in our composite dataset mean that these boundary effects can manifest across a much broader luminosity range. In this work, to facilitate direct comparison, we have adopted the identical binning strategy as Šlaus et al. (2024). As a consequence, the binned PC estimates may show localized bin-to-bin features (including apparent “bumps”) that depend on the adopted binning and on the crossing of multiple flux-limit boundaries, whereas our parametric curves are intentionally smooth and are not expected to reproduce every such local fluctuation.

A second, related factor is that the PC estimator does not explicitly account for the intrinsic distribution of spectral indices. The visibility of a source depends not only on its luminosity and redshift but also on its spectral index via the K-correction. In bins intersected by the flux-limit curves, sources with ‘unfavorable’ spectral indices (i.e., those resulting in lower observed fluxes) may fall below the detection threshold, even if they theoretically reside within the accessible (L, z) volume defined by a mean spectral index. While our trivariate parametric models fully integrate over this α -distribution to predict the total space density, the PC estimator simply counts the detected sources without compensating for this spectral-dependent incompleteness. We note that the classical $1/V_{\text{max}}$ estimator (Schmidt 1968) is subject to the identical limitation. This inevitably leads to an underestimation of the luminosity function in these boundary-crossing bins (see Yuan et al. 2016b), further explaining why the PC data points frequently lie below our model curves. In individual boundary-crossing bins, these effects can also introduce additional bin-to-bin structure in the binned estimates.

Finally, we examine the behavior of our trivariate LDDE model (purple dash-dotted line). Note that the pronounced “bump” discussed below is a feature of the LDDE fit itself, and is distinct from any localized bin-to-bin structure that may appear in the binned PC points. At lower redshifts ($z \lesssim 1.5$), this model shows good agreement with our LADE predictions. However, as redshift increases, the complex effects of luminosity-dependent density evolution become increasingly prominent. Specifically, the LDDE model begins to predict space densities exceeding those of the LADE framework at the faint end ($\log L \lesssim 25$). Most notably, a significant ‘bump’ emerges in the intermediate luminosity

range ($26 \lesssim \log L \lesssim 27$), which is immediately followed by a steeper decline at the bright end. This dramatic variation in the shape of the luminosity function suggests a scenario where low- and high-luminosity sources undergo markedly different evolutionary trajectories. However, the PC estimates do not appear to support such a scenario.

This visual assessment is strongly corroborated by the quantitative model selection criteria. The resulting AIC and BIC values are summarized in the left panel of Table 2. We find that the LADE framework provides a statistically superior description of the data compared to the LDDE parameterization, which yields significantly higher information criterion values ($\Delta\text{AIC} > 700$ relative to Model C). Among the three LADE variants, Model C consistently achieves the lowest AIC and BIC scores. This indicates that the LADE model with flexible density and luminosity evolution (Model C) offers the most parsimonious representation of the cosmic evolution of steep-spectrum radio-loud AGNs, optimally balancing goodness-of-fit with model complexity.

4.2. Robustness of the Evolutionary Model

A potential concern in modeling the high-redshift evolution is the impact of observational selection effects. Specifically, at $z \gtrsim 3.5$, our composite sample is dominated by deep, pencil-beam surveys (e.g., COSMOS), which may lack the volume to detect rare, high-luminosity sources. One might suspect that the statistical preference for Model C—which allows for a flexible turnover in density and luminosity evolution—is primarily driven by the need to accommodate this high-redshift truncation.

To test the robustness of our results, we performed a sensitivity analysis by repeating the MCMC fitting procedure on a restricted subset of data with $z < 3.5$, where the coverage in the luminosity-redshift plane is most complete. The resulting AIC values for this subset are summarized in the right panel of Table 2.

Remarkably, Model C remains the statistically preferred description, with a ΔAIC of 22.4 relative to Model B. This confirms that the complex evolutionary trends captured by Model C (including the non-monotonic behavior in luminosity or the flattening in density evolution) are already firmly established by the high-quality data around ‘cosmic noon’ ($z \sim 1 - 3$) and are not merely artifacts of the sparse sampling at the highest redshifts. Consequently, we conclude that Model C is the statistically preferred model, effectively characterizing the evolutionary behavior of radio-loud AGNs.

4.3. Consistency with Observed Source Counts

An important consistency check for any parametric RLF model is its ability to reproduce the observed SCs $n(F_\nu)$. We calculate the SCs for each of our three LADE model LFs using Equation (9). The results are presented in Figure 5, where the blue, orange and green dash-dotted lines correspond to Models A, B, and C, respectively. In this figure, we compare our models with the Euclidean-normalized 1.4 GHz SCs for AGNs compiled from de Zotti et al. (2010), Padovani et al. (2015), Smolčić et al. (2017b), Algera et al. (2020), and Hale et al. (2023). All three models reproduce these SCs closely in the bright regime ($F_\nu > 1$ mJy). Below 1 mJy, the observed counts show a systematic excess relative to the model predictions. This discrepancy is likely attributable to residual contamination from SFGs in the observational samples.

4.4. Density and Luminosity Evolution

Figure 6 summarizes the inferred evolution of the DE and LE functions for Models A–C. The upper panels display these evolutionary trends as a function of redshift (z), while the lower panels present them as a function of cosmic age (t). In the context of our LADE framework, these two components play distinct physical roles: the LE function, $e_2(z)$, describes the evolution of the characteristic luminosity scale (shifting the “knee” of the luminosity function, $L_* \rightarrow L_* e_2(z)$), whereas the DE function, $e_1(z)$, governs the evolution of the global normalization (ϕ_*) at a fixed luminosity.

As observed in the upper panels, across all three models, the LE term exhibits a strong positive evolution from $z \simeq 0$ to the “cosmic noon” epoch ($z \sim 2$), indicating a rapid increase in the characteristic radio power of steep-spectrum AGNs toward earlier cosmic times. Model A continues a monotonic rise by construction because it adopts a simple power-law form for $e_2(z)$. However, Models B and C, which allow for redshift-dependent indices, reveal a saturation or mild turnover in the characteristic luminosity at $z \geq 3.5$. This suggests that the typical luminosity of radio AGNs does not grow indefinitely but likely plateaus during the epoch of initial supermassive black hole assembly.

In contrast to the rising LE, all models favor a negative DE with increasing redshift, indicating a systematic decline in the LF normalization toward earlier epochs. For Models A and B, this decrease is explicitly exponential in z via the

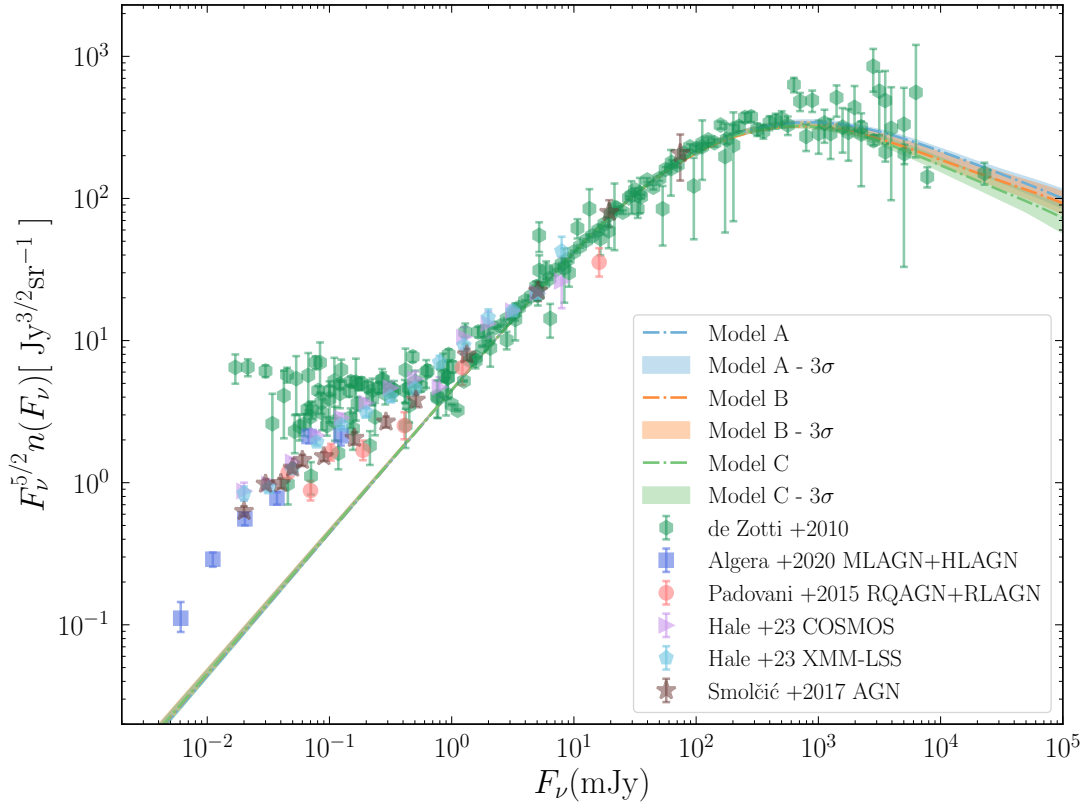


Figure 5. Comparison of our best-fit models with the Euclidean normalized 1.4 GHz SCs for AGNs observed in the literature. The blue, orange, and green dash-dotted lines show our best-fit SCs of Models A, B, and C, respectively. The SCs from Hale et al. (2023) in the COSMOS and XMM-LSS fields are shown as brown right triangles and cyan pentagons, respectively. Also shown are the observed SCs from Smolčić et al. (2017b) (brown five-pointed stars), Algera et al. (2020) (blue squares), and Padovani et al. (2015) (red circles), with associated error bars in all cases.

adopted $e_1(z) = \exp(-p_1 z)$ form, while Model C permits additional flexibility and shows a slower decline at $z \geq 2.5$. Consequently, the evolution of steep-spectrum AGNs is best described by a “dual” process: a decrease in the overall number density of sources, counterbalanced by a significant increase in their intrinsic luminosities.

We emphasize that while DE and LE are mathematically distinct in Equation (10), their physical decoupling provides key insights into AGN growth. The monotonic decline of $e_1(z)$ implies that the total comoving number density of steep-spectrum AGNs decreases toward higher redshift. Meanwhile, the rapid rise of $e_2(z)$ up to $z \sim 2 - 3$ indicates that although these sources are rarer in the early Universe, they are systematically more powerful. This is consistent with a scenario where high-redshift radio galaxies represent a phase of highly efficient fueling and rapid black hole growth, coinciding with the peak of cosmic star formation activity.

We stress that the DE/LE trends inferred here describe an effective global evolution of the full steep-spectrum radio-loud AGN sample treated as a single statistical population. This does not imply that radio-loud AGNs arise from a single physical accretion/feedback mode, nor does it rule out an underlying bimodality (e.g. high-/low-excitation radio galaxies or cold-/hot-mode accretion). Rather, our results indicate that, for the radio-only LF of the steep-spectrum (FSRQ-excluded) sample, the data do not require two independent evolutionary tracks: any distinct physical modes may substantially overlap in radio luminosity and redshift, or their relative contributions may vary smoothly with (z, L) , yielding the observed smooth DE and LE behavior. A direct test of physical bimodality would require modelling the LFs separately for physically classified subsamples, which we defer to future work.

4.5. Luminosity-dependent Evolution

As discussed by Rigby et al. (2015) and Yuan et al. (2016a); Yuan et al. (2017), the position of the steep-spectrum RLF peak is luminosity dependent; specifically, the comoving space density of the most powerful sources peaks at higher redshift than that of their weaker counterparts. Figure 7 illustrates the redshift evolution of the comoving

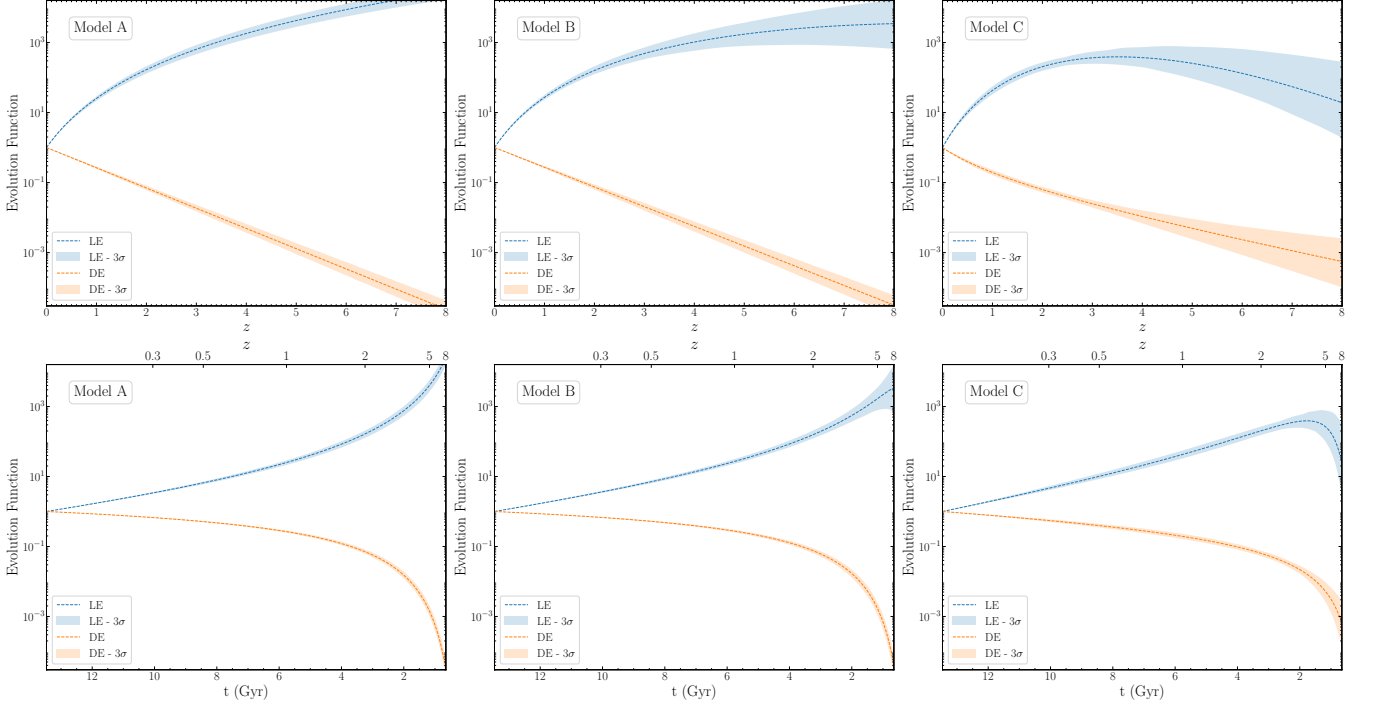


Figure 6. Evolution of the density (orange) and luminosity (blue) functions for Models A, B, and C. Top panels show the evolution as a function of redshift (z), while bottom panels display the evolution as a function of cosmic age (t , in Gyr). The lightly shaded regions indicate the 3σ confidence intervals.

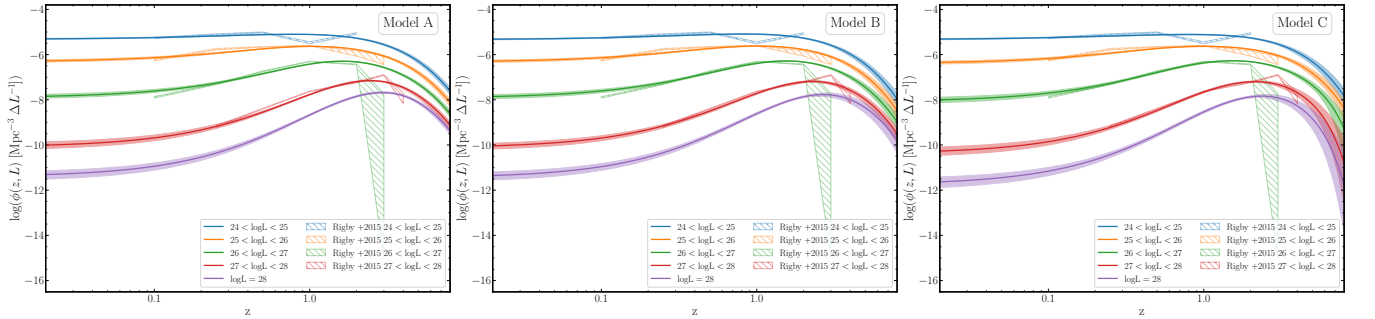


Figure 7. Redshift evolution of the comoving space density for Models A, B, and C. The blue, orange, green, red, and purple solid lines represent the radio RLFs at $\log(L_{1.4 \text{ GHz}} [\text{W Hz}^{-1}]) = 24.5, 25.5, 26.5, 27.5,$ and 28.0 , respectively. The shaded regions indicate the 3σ uncertainty ranges. For comparison, the results from Rigby et al. (2015) are shown as blue, orange, green, and red hatched regions.

space density for Models A, B, and C at various luminosities. The inferred evolution exhibits a clear signature of “cosmic downsizing”: the evolutionary trends are strongly dependent on radio luminosity. Moreover, the amplitude of the evolution from $z = 0$ to the redshift at which the space density peaks is also highly luminosity-dependent. For high-luminosity sources, the variation in space density spans more than two orders of magnitude, whereas for low-luminosity sources, the change is less than an order of magnitude. This behavior is consistent with what has been observed for quasars (QSOs) selected in the X-ray and optical bands (e.g., Hasinger et al. 2005; Hopkins et al. 2007).

For comparison, we also show the results from Rigby et al. (2015) in Figure 7. Our model predictions are in good agreement with Rigby et al. (2015). However, it is worth noting that in the luminosity range $24 < \log L < 25$, the radio LF from Rigby et al. (2015) exhibits a noticeable dip around $z \sim 1$. This feature is unlikely to represent a real decline in space density; rather, it may be an artifact arising from the sensitivity of binned estimators to bin placement

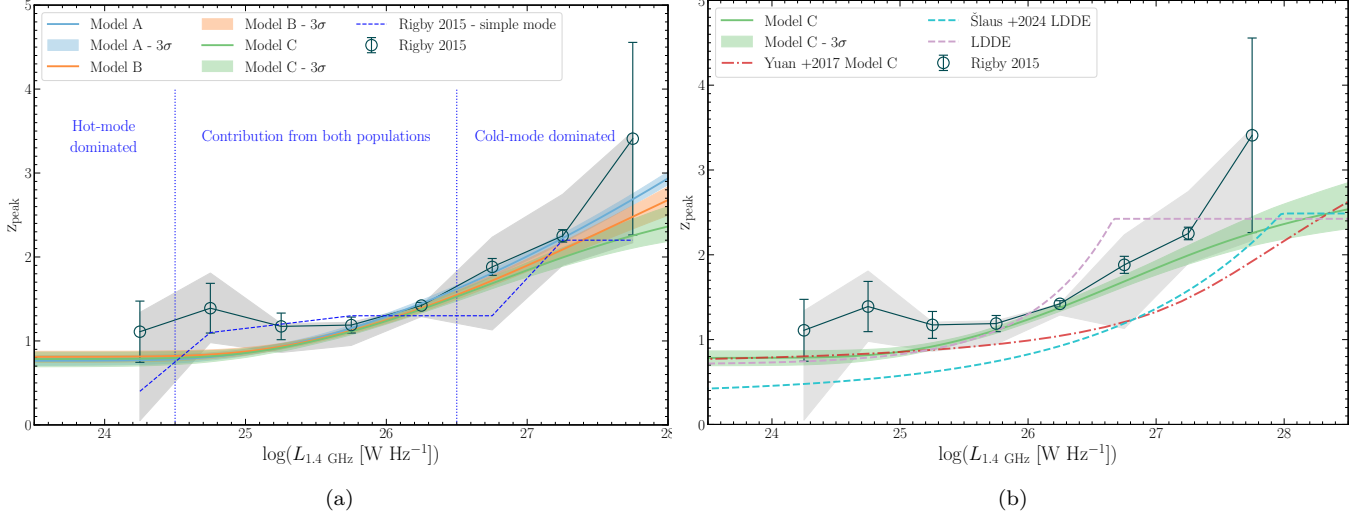


Figure 8. Variation in the redshift of the peak space density with radio luminosity and comparisons with literature results. **(a)** The blue, orange, and green dashed lines represent our Models A, B, and C, respectively, with shaded regions indicating the 3σ confidence intervals. The red dash-dotted line shows the prediction from Model C of Yuan et al. (2017), while the dark blue circles with error bars denote the results from Rigby et al. (2015). The grey shaded area illustrates the range in their results found by varying the input parameters in the RLF grid modelling. The blue dashed line corresponds to the simple evolutionary model proposed in Rigby et al. (2015). **(b)** The green solid line indicates our Model C, with the surrounding shaded area marking its 3σ uncertainty. The red dotted line represents Model C from Yuan et al. (2017), and the circular markers with error bars show the R15 measurements. The light blue dashed line corresponds to the LDDE model from Šlaus et al. (2024), while the purple dashed line shows the LDDE model in this work, both with shaded regions indicating their respective 3σ confidence intervals.

and widths. As pointed out by Yuan & Wang (2013), such binning-based estimates are highly sensitive to the choice of bin edges and widths.

4.6. Luminosity-dependent z_{peak}

Figure 8 shows the redshift at which the total comoving space density at fixed luminosity reaches its maximum, z_{peak} , as a function of radio luminosity. In panel (a), we compare our three LADE models with the reference result of Rigby et al. (2015). The blue, green, and orange dashed lines represent the predictions from Models A, B, and C, respectively, with shaded regions indicating the corresponding 3σ confidence intervals. The dark blue open circles with error bars show the nonparametric results from Rigby et al. (2015). Given the grid-based modeling approach adopted in that work (see original paper for details), the uncertainties arising from variations in input parameters are indicated by the grey shaded area. Our model predictions lie almost entirely within this region, demonstrating excellent consistency between our measurements and those of Rigby et al. (2015). Furthermore, the overall trend in z_{peak} predicted by our models agrees very well with their results.

We also plot the simple evolutionary model proposed by Rigby et al. (2015) as the blue dashed line. This model assumes two dominant accretion modes in radio galaxies—cold-mode and hot-mode accretion. Cold-mode sources, typically high-luminosity AGNs, are powered by radiatively efficient accretion of cold gas (e.g., galaxy mergers), and their comoving density rises rapidly with redshift, peaking at a luminosity-dependent high redshift ($z \sim 2\text{--}4$) before declining sharply. Hot-mode sources, by contrast, are associated with radiatively inefficient accretion of hot halo gas and exhibit a peak in space density around $z \sim 0.8$, with a much milder evolutionary trend that shows little dependence on luminosity. The total evolution is constructed by summing the two components at each luminosity, and we therefore define $z_{\text{peak}}(L)$ using this summed density (not the individual components, which may peak at different redshifts). Remarkably, our LADE model predictions closely track the trajectory of this dual-mode scenario. This suggests that the LADE framework can phenomenologically capture the transition from hot-mode to cold-mode dominance with a single parametric form, without requiring an explicit decomposition into two populations.

In panel (b), we adopt our preferred LADE Model C as the baseline and compare it with other published determinations. The red dash-dotted line shows Model C from Yuan et al. (2017), which also employs the LADE formalism.

While the overall trend is consistent, an offset is apparent. We attribute this primarily to the substantial improvement in sample statistics and phase-space coverage achieved here: our sample is ~ 4 times larger than that of Yuan et al. (2017), and, crucially, the inclusion of the XXL and COSMOS surveys provides much tighter constraints on the faint end that were previously less well determined. As a result, the present $z_{\text{peak}}(L)$ relation should be viewed as a robust refinement of the earlier estimates. In addition, to a lesser extent, systematic uncertainties arising from the conversion of the 408 MHz RLF to 1.4 GHz (assuming a fixed spectral index $\alpha = 0.75$) in Yuan et al. (2017) may also contribute to the observed offset.

Panel (b) also compares our LADE result with the LDDE-based predictions. The light blue dashed line shows the LDDE result from Šlaus et al. (2024), while the purple dashed line corresponds to the LDDE fit obtained in this work. Crucially, neither of these LDDE parameterizations reproduces the non-parametric results of Rigby et al. (2015) as faithfully as our LADE model. Moreover, the LDDE forms exhibit an artificial feature where the rise of z_{peak} abruptly saturates into a flat plateau at high luminosities. In contrast, the LADE model yields a smooth, continuous dependence that appears more physically plausible.

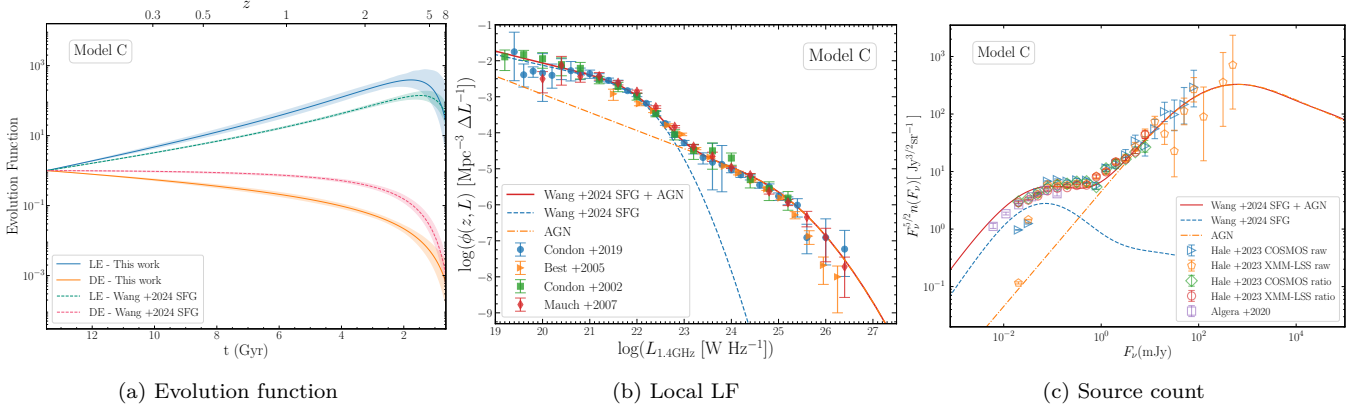


Figure 9. Unified two-component description of the 1.4 GHz radio population under Model C. (a) Evolution functions versus cosmic age t . Solid lines: AGN DE (blue) and LE (orange). Dashed lines: SFG DE (green) and LE (pink) from W24. Shading shows the 3σ confidence intervals. (b) Local ($z = 0.1$) RLFs for SFGs (green dashed) and AGNs (orange dash-dotted) and their sum (total; red solid), compared to the local measurements of Condon et al. (2019), Best et al. (2005), Condon et al. (2002), and Mauch & Sadler (2007). (c) Euclidean-normalized differential source counts at 1.4 GHz for SFGs (green dashed) and AGNs (orange dash-dotted) and their sum (total; red solid), compared with the COSMOS/XMM-LSS counts of Hale et al. (2023) and the measurements of Algra et al. (2020).

5. DISCUSSION

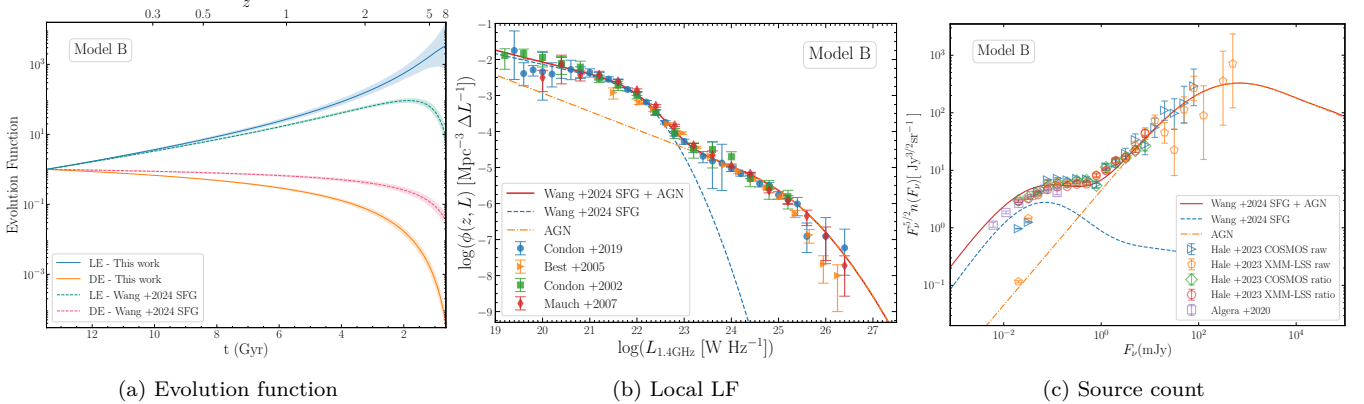


Figure 10. Same as Figure 9, but for Model B.

5.1. *A Unified Evolutionary Framework for AGNs and SFGs*

Having established a LADE-based description of the radio-loud AGN LF, we now cast it in the same parametric framework used to model the SFG radio LF in our previous work (Wang et al. 2024, hereafter W24). Although the AGN and SFG analyses were conducted independently, the preferred prescriptions identified in the two studies—Models B and C for AGNs and the W24 model for SFGs—converge on an identical mathematical architecture. In particular, they adopt the same family of local LFs and employ the same functional forms for DE and LE.

Importantly, this concordance was not enforced a priori. In fitting the AGN sample, we tested a broad suite of candidate DE/LE parameterizations and retained Models B and C solely on statistical grounds, i.e., their favorable balance between goodness-of-fit and parsimony as quantified by information criteria (e.g., AIC). That the resulting AGN models coincide with the SFG prescriptions from W24 therefore emerges a posteriori, providing a rigorous and standardized “common language” for controlled comparisons between these physically distinct populations.

We next focus on our fiducial unified description under Model C, presented in Figure 9. Panel (a) compares the best-fitting DE and LE terms for the SFG component from W24 and the steep-spectrum AGN component derived here. Despite the fact that the two populations are governed by distinct parameter values, their inferred LE histories are broadly similar: the characteristic luminosities rise toward a maximum at $z \sim 2\text{--}3$ and then flatten or exhibit a mild decline at higher redshift. By contrast, the DE terms decrease with redshift for both populations, remaining monotonic over the redshift range probed. Overall, the two components display qualitatively consistent evolutionary trends within the same LADE functional family, while retaining population-specific amplitudes and detailed redshift dependences.

A closer comparison, however, reveals systematic differences in the strength of the evolution. In the rising phase toward cosmic noon, the AGN LE increases more steeply than that of SFGs, implying a more rapid brightening of the characteristic radio power with redshift. This behavior is qualitatively consistent with the expectation that the processes governing radio-loud AGN activity—e.g., the availability of fuel for SMBH accretion and the triggering of powerful jets—are more strongly peaked in time around $z \sim 2\text{--}3$ than the mechanisms regulating star formation in the general galaxy population, which evolve more smoothly.

The contrast is even more pronounced in the DE term: the AGN DE declines faster with redshift than the SFG DE over the same interval. Within the LADE decomposition, this indicates that the comoving abundance (or, equivalently, the effective duty cycle) of the radio-loud AGN population decreases more rapidly toward earlier cosmic times than that of SFGs. Taken together, the steeper LE rise and the faster DE decline suggest that, although both populations can be described within a unified functional framework, radio-loud AGNs exhibit a stronger redshift dependence—i.e., a more pronounced cosmological evolution—than SFGs in Model C.

Panel (b) of Figure 9 shows the implied local ($z = 0.1$) 1.4 GHz RLFs for the two components and their sum. Specifically, we combine the steep-spectrum AGN LF inferred under our Model C with the SFG LF from W24 (also under Model C) to obtain the total RLF (red solid curve). The resulting total RLF agrees well with a range of independent local measurements, including those from Condon et al. (2019), Best et al. (2005), Condon et al. (2002), and Mauch & Sadler (2007), indicating that the unified decomposition provides a consistent description of both the faint and bright ends of the local radio population. Panel (c) presents an analogous comparison in terms of the Euclidean-normalized differential source counts. Here we sum the SFG and AGN contributions predicted by the unified Model C to obtain the total 1.4 GHz radio counts, and compare them with observational determinations from Hale et al. (2023) and Algera et al. (2020). The combined model reproduces both the overall normalization and the flux-dependent curvature of the observed counts over the full range probed, indicating that the same two-component decomposition that matches the local LF also provides a self-consistent description of the global source-count statistics.

Figure 10 presents the same unified, two-component decomposition as Figure 9, but adopting Model B. The overall behavior is unchanged: the AGN and SFG evolution functions remain broadly consistent within the shared LADE architecture, their summed local ($z = 0.1$) RLF continues to match the published $z \approx 0$ measurements, and the combined Euclidean-normalized source counts reproduce the observed normalization and curvature over the relevant flux-density range. Consequently, the main qualitative trends inferred from Model C remain unchanged when adopting Model B, indicating that our conclusions are not sensitive to the choice between these two preferred parameterizations. We nevertheless adopt Model C as our fiducial model because it yields slightly better information-criterion values.

The similarity of the inferred LE and DE trends for SFGs and radio-loud AGNs provides a useful population-level baseline for co-evolution studies, while not by itself implying a direct, galaxy-by-galaxy causal link between star formation and accretion.

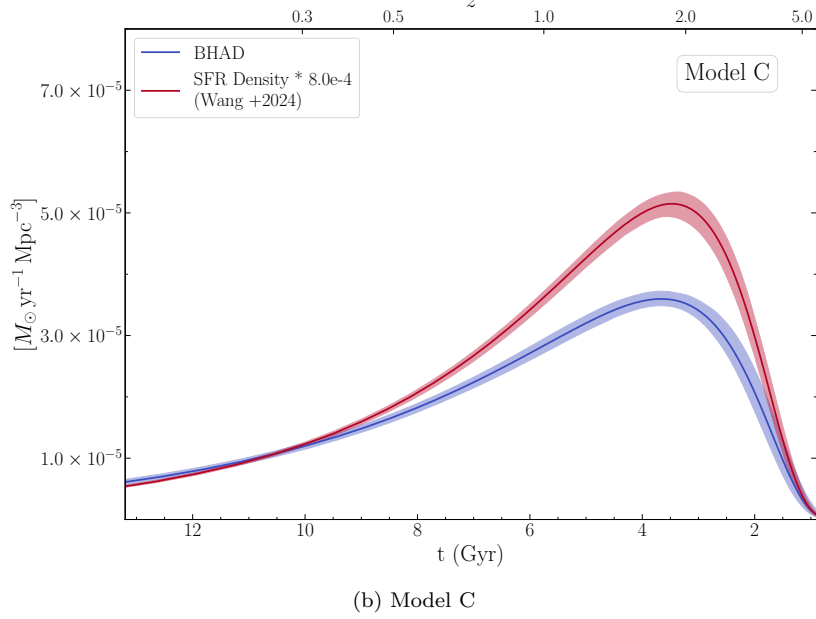


Figure 11. Cosmic evolution of the BHAD (blue) compared with the SFRD (red) derived from our previous work (Wang et al. 2024). The SFRD has been rescaled by a factor of 0.8×10^{-3} following Heckman & Best (2014) to enable direct comparison with the BHAD. Solid curves denote the best-fit predictions, while shaded regions indicate the associated 3σ uncertainties.

5.2. Deriving the Black Hole Accretion Rate Density

Having derived the rest-frame 1.4 GHz LF, we are able to derive the BHAD (Ψ_{bhar}) over cosmic time, from $z \sim 4$ down to the present epoch. Following Šlaus et al. (2024) (see also Smolčić et al. 2017a; Ceraj et al. 2018), we determined the kinetic luminosity from the radio luminosity using the relation

$$\log L_{\text{kin}} = 0.86 \log L_{1.4 \text{ GHz}} + 14.08 + 1.5 \log f_{\text{W}}, \quad (19)$$

where L_{kin} is the kinetic luminosity, $L_{1.4 \text{ GHz}}$ is the rest-frame 1.4 GHz radio luminosity, and f_{W} is a parameter introduced by Willott et al. (1999) to account for all possible systematic uncertainties. Based on observational constraints, f_{W} is typically estimated to lie in the range 1–20. We assumed $f_{\text{W}} = 15$, for which the Willott et al. (1999) relation is consistent with jet kinetic luminosities inferred from X-ray cavity observations in galaxy groups and clusters (Bîrzan et al. 2004; O’Sullivan et al. 2011; Smolčić et al. 2017a; Ceraj et al. 2018; Šlaus et al. 2024); this parameter introduces only a multiplicative normalization shift in the kinetic luminosity density, leaving the redshift dependence unchanged.

Using Equation (19), we derive the kinetic LF as

$$\Phi(L_{\text{kin}}, z) d \log L_{\text{kin}} = \Phi_{1.4 \text{ GHz}}(L_{1.4 \text{ GHz}}, z) d \log L_{1.4 \text{ GHz}}, \quad (20)$$

where the transformation follows from the logarithmic relation in Equation (19). The BHAD is then computed using a “Sołtan-type” argument:

$$\Psi_{\text{bhar}}(z) = \int_0^{\infty} d \log L_{\text{kin}} \Phi(L_{\text{kin}}, z) \frac{(1 - \epsilon_{\text{rad}} - \epsilon_{\text{kin}}) L_{\text{kin}}}{\epsilon_{\text{kin}} c^2}, \quad (21)$$

where $\Phi(L_{\text{kin}}, z)$ is the kinetic LF obtained from the radio LF via Equation (20), and ϵ_{rad} and ϵ_{kin} are the radiative and kinetic efficiencies, respectively (Sołtan 1982; Shankar et al. 2008). In this expression, the last term represents the total mass accreted onto the central black hole for a source of kinetic luminosity L_{kin} , i.e., the individual black hole accretion rate

$$\dot{M}_{\text{BH}} = \frac{(1 - \epsilon_{\text{rad}} - \epsilon_{\text{kin}}) L_{\text{kin}}}{\epsilon_{\text{kin}} c^2}; \quad (22)$$

see Shankar et al. (2008) for a detailed derivation.

We adopt $\epsilon_{\text{rad}} = 0.1$ and $\epsilon_{\text{kin}} = 0.003$ in Equation (21). The radiative efficiency $\epsilon_{\text{rad}} = 0.1$ is a widely used fiducial choice and is broadly consistent with Soltan-type constraints that relate the time-integrated AGN emissivity to the local black hole mass density (Soltan 1982; Hopkins et al. 2007; Shankar et al. 2008; Delvecchio et al. 2014). For example, Shankar et al. (2008) found a mass-weighted mean $\epsilon_{\text{rad}} \sim 0.07\text{--}0.1$ from multiwavelength AGN synthesis modeling, and Delvecchio et al. (2014) adopted $\epsilon_{\text{rad}} = 0.1$ when converting IR-based AGN luminosities into accretion rates, obtaining a BHAD evolution consistent with the local black hole mass density.

Our choice of $\epsilon_{\text{kin}} = 0.003$ is motivated by empirical and synthesis-model estimates of jet kinetic power in radio AGNs. Merloni & Heinz (2008) inferred typical kinetic efficiencies of $\epsilon_{\text{kin}} \simeq (3\text{--}5) \times 10^{-3}$ (with dependencies on black hole mass and redshift) and showed that such values can supply the energy required for maintenance-mode feedback in massive halos. While higher values (up to $\sim 10^{-2}$) have also been advocated for radio-loud sources under specific assumptions (e.g., Shankar et al. 2008), the inferred efficiencies remain subject to systematic uncertainties (e.g., bolometric corrections, obscured fractions, and jet coupling). Adopting $\epsilon_{\text{rad}} = 0.1$ and $\epsilon_{\text{kin}} = 0.003$ therefore provides a conservative, literature-supported baseline. The resulting BHAD evolution from our fiducial Model C is shown in Figure 11 and discussed in detail in the next subsection.

5.3. Co-evolution of BHAD and SFRD

To place the inferred BHAD evolution in a broader galaxy-evolution context, we compare it with the cosmic SFRD. For the SFRD we adopt the radio-based reconstruction from our previous work (W24), derived from the Model C fit to the SFG RLF. This ensures that both the SFRD and BHAD comparisons are anchored to the same LF functional family. Following the convention of Heckman & Best (2014), we rescale the SFRD by a factor of 0.8×10^{-3} to facilitate a direct, shape-based comparison with the BHAD (i.e., to visualize the approximately constant SFRD-to-BHAD ratio reported at the population level).

To enable a meaningful comparison with the BHAD, we rescaled the SFRD by a factor of 0.8×10^{-3} , following the convention adopted in Heckman & Best (2014), who noted that the ratio between star formation and black hole accretion has remained approximately constant over cosmic time, with a value of order 10^3 . The comparison is illustrated in Figure 11, where the blue and red solid lines represent the evolution of the BHAD and the rescaled SFRD, respectively. The shaded regions show the associated 3σ uncertainties. A remarkable similarity is observed between the two evolutionary tracks: both the BHAD and the SFRD exhibit a pronounced rise from the local Universe toward higher redshift, peaking around $z \sim 2$, an epoch commonly referred to as the “cosmic noon”. This consistency suggests a close link between the growth of stellar mass and black hole mass in galaxies, supporting the idea that the mechanisms driving star formation and SMBH accretion may be tightly coupled throughout cosmic history.

A further advantage of our approach is methodological consistency: the SFG LF models used in W24 (Models B and C) share the same functional form as the AGN LF models adopted here, differing only in their best-fitting parameters for each population. Thus, a single parametric LF framework can simultaneously describe two physically distinct components—SFGs and radio-loud AGNs—over a wide redshift range. This remarkable agreement underscores the robustness and versatility of our LF framework, and may further imply that the cosmic evolution of star formation and black hole growth are governed by common underlying processes (also see Heckman & Best 2014; Madau & Dickinson 2014), possibly regulated by large-scale gas accretion and feedback mechanisms (Croton et al. 2006; Hopkins et al. 2006).

6. CONCLUSIONS

We have presented a comprehensive study of the cosmic evolution of radio-loud active galactic nuclei (AGNs) using a beaming-minimized sample of 4,555 steep-spectrum sources. By adopting a luminosity and density evolution (LADE) framework that separates luminosity evolution (LE) and density evolution (DE), we derive a unified and physically transparent description of the AGN radio luminosity function (RLF) at 1.4 GHz over $0 < z \lesssim 4$. Our main conclusions are as follows:

1. *A LADE description is strongly supported by the data.* Following the LADE framework of Yuan et al. (2017), we find that the cosmic evolution of steep-spectrum radio-loud AGNs can be well described by a separable combination of DE and LE applied to a flexible local LF family. The best-fitting models reproduce the binned RLFs and are simultaneously consistent with external constraints from the local RLFs and Euclidean-normalized source counts, yielding a globally self-consistent description across the full dynamic range of our composite sample. In our fiducial Model C, the LE term increases toward cosmic noon ($z \sim 2\text{--}3$) and then flattens or

mildly declines at higher redshift, whereas the DE term decreases monotonically with redshift over the range probed.

2. *The observed luminosity-dependent peak redshift is naturally captured by the LADE framework.* Our LADE (DE+LE) model reproduces the luminosity-dependent turnover (or peak) redshift $z_{\text{peak}}(L)$ inferred from the data—the phenomenology often referred to as “cosmic downsizing.” Importantly, within this framework there is no need to impose *a priori* different evolutionary laws for low- and high-power radio-loud AGNs; the apparent luminosity dependence arises self-consistently from the same underlying DE and LE terms acting on an LF whose slope changes with luminosity.
3. *A unified functional architecture describes both star-forming galaxies (SFGs) and AGNs.* A key result is that the same LADE functional family previously calibrated for SFGs in W24 also provides an excellent description of radio-loud AGNs when fitted independently. This posteriori convergence enables controlled, like-for-like comparisons between the two physically distinct populations within a standardized parametric framework.
4. *The unified two-component model is globally self-consistent.* Combining the SFG component from W24 (Model C) with our AGN component (Model C) yields a total 1.4 GHz RLF and source counts that agree well with the corresponding observational benchmarks, supporting the internal consistency of the two-component decomposition at both the LF and source-count level.
5. *The black hole accretion rate density (BHAD) inferred from radio-mode accretion tracks the cosmic star formation rate density (SFRD) in shape.* Using a radio-to-kinetic conversion (with $f_W = 15$) and standard efficiency parameters, we derive the kinetic (radio-mode) BHAD. The resulting BHAD evolution closely follows the redshift dependence of the radio-based SFRD from W24 (after a conventional rescaling), with both histories rising toward and peaking near $z \sim 2$. This population-level synchronization is consistent with a regulated co-evolution picture, while not by itself establishing a one-to-one causal coupling within individual galaxies.

Looking ahead, the dominant uncertainties at $z \gtrsim 3$ and in the radio-to-kinetic conversion primarily affect the normalization of the BHAD rather than the qualitative shape of its redshift evolution. Future deep, wide-field surveys with facilities such as the SKA and the VLA will be essential for tightening constraints on the faint end and high-redshift regime, providing stringent tests of the unified evolutionary framework developed here.

In summary, our results support a compact LADE-based description that simultaneously captures the radio evolution of both star formation and radio-loud AGN activity, and offers a consistent route to link the kinetic output of SMBHs to the global history of galaxy growth.

- 1 We acknowledge financial support from the Science Fund for Distinguished Young Scholars of Hunan Province (Grant
- 2 No. 2024JJ2040), the National Natural Science Foundation of China (Grant Nos. 12073069, 12075084, 12275080,
- 3 and 12393813), the Major Basic Research Project of Hunan Province (Grant No. 2024JC0001), and the Innovative
- 4 Research Group of Hunan Province (Grant No. 2024JJ1006). Z.Y. is supported by the Xiaoxiang Scholars Programme
- 5 of Hunan Normal University. We thank R. K. Cochrane for insightful discussions and valuable guidance on the data
- 6 classification process.

REFERENCES

- Aird, J., Nandra, K., Laird, E. S., et al. 2010, MNRAS, 401, 2531, doi: [10.1111/j.1365-2966.2009.15829.x](https://doi.org/10.1111/j.1365-2966.2009.15829.x)
- Ajello, M., Shaw, M. S., Romani, R. W., et al. 2012, ApJ, 751, 108, doi: [10.1088/0004-637X/751/2/108](https://doi.org/10.1088/0004-637X/751/2/108)
- Akaike, H. 1974, IEEE Transactions on Automatic Control, 19, 716
- Algera, H. S. B., van der Vlugt, D., Hodge, J. A., et al. 2020, ApJ, 903, 139, doi: [10.3847/1538-4357/abb77a](https://doi.org/10.3847/1538-4357/abb77a)
- Beifiori, A., Courteau, S., Corsini, E. M., & Zhu, Y. 2012, MNRAS, 419, 2497, doi: [10.1111/j.1365-2966.2011.19903.x](https://doi.org/10.1111/j.1365-2966.2011.19903.x)
- Best, P., Kauffmann, G., Heckman, T., & Ivezić, Ž. 2005, Monthly Notices of the Royal Astronomical Society, 362, 9
- Best, P. N., Arts, J. N., Röttgering, H. J. A., et al. 2003, MNRAS, 346, 627, doi: [10.1046/j.1365-2966.2003.07125.x](https://doi.org/10.1046/j.1365-2966.2003.07125.x)

- Best, P. N., Röttgering, H. J. A., & Lehnert, M. D. 1999, MNRAS, 310, 223, doi: [10.1046/j.1365-8711.1999.02984.x](https://doi.org/10.1046/j.1365-8711.1999.02984.x)
- . 2000, MNRAS, 315, 21, doi: [10.1046/j.1365-8711.2000.03319.x](https://doi.org/10.1046/j.1365-8711.2000.03319.x)
- Birzan, L., Rafferty, D. A., McNamara, B. R., Wise, M. W., & Nulsen, P. E. J. 2004, ApJ, 607, 800, doi: [10.1086/383519](https://doi.org/10.1086/383519)
- Botev, Z. I., Grotowski, J. F., & Kroese, D. P. 2010, Annals of Statistics, 38, doi: [10.1214/10-AOS799](https://doi.org/10.1214/10-AOS799)
- Bower, R. G., Benson, a. J., Malbon, R., et al. 2006, MNRAS, 370, 645, doi: [10.1111/j.1365-2966.2006.10519.x](https://doi.org/10.1111/j.1365-2966.2006.10519.x)
- Boyle, B. J., Shanks, T., Croom, S. M., et al. 2000, MNRAS, 317, 1014, doi: [10.1046/j.1365-8711.2000.03730.x](https://doi.org/10.1046/j.1365-8711.2000.03730.x)
- Brookes, M. H., Best, P. N., Peacock, J. A., Röttgering, H. J. A., & Dunlop, J. S. 2008, MNRAS, 385, 1297, doi: [10.1111/j.1365-2966.2008.12786.x](https://doi.org/10.1111/j.1365-2966.2008.12786.x)
- Butler, A., Huynh, M., Delhaize, J., et al. 2018, A&A, 620, A3, doi: [10.1051/0004-6361/201630129](https://doi.org/10.1051/0004-6361/201630129)
- Ceraj, L., Smolčić, V., Delvecchio, I., et al. 2018, A&A, 620, A192, doi: [10.1051/0004-6361/201833935](https://doi.org/10.1051/0004-6361/201833935)
- Clarke, D. A., Harris, D. E., & Carilli, C. L. 1997, MNRAS, 284, 981, doi: [10.1093/mnras/284.4.981](https://doi.org/10.1093/mnras/284.4.981)
- Clewley, L., & Jarvis, M. J. 2004, MNRAS, 352, 909, doi: [10.1111/j.1365-2966.2004.07981.x](https://doi.org/10.1111/j.1365-2966.2004.07981.x)
- Cochrane, R. K., Kondapally, R., Best, P. N., et al. 2023, MNRAS, 523, 6082, doi: [10.1093/mnras/stad1602](https://doi.org/10.1093/mnras/stad1602)
- Condon, J. J. 1984, ApJ, 284, 44, doi: [10.1086/162382](https://doi.org/10.1086/162382)
- Condon, J. J., Cotton, W. D., & Broderick, J. J. 2002, AJ, 124, 675, doi: [10.1086/341650](https://doi.org/10.1086/341650)
- Condon, J. J., Matthews, A. M., & Broderick, J. J. 2019, ApJ, 872, 148, doi: [10.3847/1538-4357/ab0301](https://doi.org/10.3847/1538-4357/ab0301)
- Croton, D. J., Springel, V., White, S. D. M., et al. 2006, MNRAS, 365, 11, doi: [10.1111/j.1365-2966.2005.09675.x](https://doi.org/10.1111/j.1365-2966.2005.09675.x)
- Croton, D. J., Stevens, A. R. H., Tonini, C., et al. 2016, ApJS, 222, 22, doi: [10.3847/0067-0049/222/2/22](https://doi.org/10.3847/0067-0049/222/2/22)
- D'Ammando, F., Raiteri, C. M., Villata, M., et al. 2019, MNRAS, 490, 5300, doi: [10.1093/mnras/stz2792](https://doi.org/10.1093/mnras/stz2792)
- Davé, R., Anglés-Alcázar, D., Narayanan, D., et al. 2019, MNRAS, 486, 2827, doi: [10.1093/mnras/stz937](https://doi.org/10.1093/mnras/stz937)
- de Zotti, G., Massardi, M., Negrello, M., & Wall, J. 2010, A&A Rv, 18, 1, doi: [10.1007/s00159-009-0026-0](https://doi.org/10.1007/s00159-009-0026-0)
- Delvecchio, I., Gruppioni, C., Pozzi, F., et al. 2014, MNRAS, 439, 2736, doi: [10.1093/mnras/stu130](https://doi.org/10.1093/mnras/stu130)
- Enia, A., Talia, M., Pozzi, F., et al. 2022, The Astrophysical Journal, 927, 204
- Fabian, A. C. 2012, ARA&A, 50, 455
- Fan, X., Strauss, M. A., Schneider, D. P., et al. 2001, The Astronomical Journal, 121, 54
- Ferrarese, L., & Merritt, D. 2000, ApJL, 539, L9, doi: [10.1086/312838](https://doi.org/10.1086/312838)
- Feruglio, C., Maiolino, R., Piconcelli, E., et al. 2010, A&A, 518, L155, doi: [10.1051/0004-6361/201015164](https://doi.org/10.1051/0004-6361/201015164)
- Foreman-Mackey, D., Hogg, D. W., Lang, D., & Goodman, J. 2013, Publications of the Astronomical Society of the Pacific, 125, 306
- Gebhardt, K., Bender, R., Bower, G., et al. 2000, ApJL, 539, L13, doi: [10.1086/312840](https://doi.org/10.1086/312840)
- Gendre, M. A., & Wall, J. V. 2008, MNRAS, 390, 819, doi: [10.1111/j.1365-2966.2008.13792.x](https://doi.org/10.1111/j.1365-2966.2008.13792.x)
- Graham, A. W., Onken, C. A., Athanassoula, E., & Combes, F. 2011, MNRAS, 412, 2211, doi: [10.1111/j.1365-2966.2010.18045.x](https://doi.org/10.1111/j.1365-2966.2010.18045.x)
- Hale, C. L., Whittam, I. H., Jarvis, M. J., et al. 2023, MNRAS, 520, 2668, doi: [10.1093/mnras/stac3320](https://doi.org/10.1093/mnras/stac3320)
- Hasinger, G., Miyaji, T., & Schmidt, M. 2005, A&A, 441, 417, doi: [10.1051/0004-6361:20042134](https://doi.org/10.1051/0004-6361:20042134)
- Heckman, T., & Best, P. 2014, ARA&A, 52, 589, <https://arxiv.org/abs/1403.4620>
- Hopkins, P. F., Hernquist, L., Cox, T. J., et al. 2006, ApJS, 163, 1, doi: [10.1086/499298](https://doi.org/10.1086/499298)
- Hopkins, P. F., Richards, G. T., & Hernquist, L. 2007, ApJ, 654, 731, doi: [10.1086/509629](https://doi.org/10.1086/509629)
- Jarvis, M. J., & Rawlings, S. 2000, MNRAS, 319, 121, doi: [10.1046/j.1365-8711.2000.03801.x](https://doi.org/10.1046/j.1365-8711.2000.03801.x)
- Jarvis, M. J., Rawlings, S., Willott, C. J., et al. 2001, MNRAS, 327, 907, doi: [10.1046/j.1365-8711.2001.04778.x](https://doi.org/10.1046/j.1365-8711.2001.04778.x)
- Kaviraj, S., Laigle, C., Kimm, T., et al. 2017, MNRAS, 467, 4739, doi: [10.1093/mnras/stx126](https://doi.org/10.1093/mnras/stx126)
- Kolokythas, K., O'Sullivan, E., Giacintucci, S., et al. 2015, MNRAS, 450, 1732, doi: [10.1093/mnras/stv665](https://doi.org/10.1093/mnras/stv665)
- Kondapally, R., Best, P. N., Raouf, M., et al. 2023, MNRAS, 523, 5292, doi: [10.1093/mnras/stad1813](https://doi.org/10.1093/mnras/stad1813)
- Madau, P., & Dickinson, M. 2014, ARA&A, 52, 415, doi: [10.1146/annurev-astro-081811-125615](https://doi.org/10.1146/annurev-astro-081811-125615)
- Magorrian, J., Tremaine, S., Richstone, D., et al. 1998, AJ, 115, 2285, doi: [10.1086/300353](https://doi.org/10.1086/300353)
- Marshall, H., Tananbaum, H., Avni, Y., & Zamorani, G. 1983, The Astrophysical Journal, 269, 35
- Mauch, T., & Sadler, E. M. 2007, MNRAS, 375, 931, doi: [10.1111/j.1365-2966.2006.11353.x](https://doi.org/10.1111/j.1365-2966.2006.11353.x)
- McConnell, N. J., & Ma, C.-P. 2013, ApJ, 764, 184, doi: [10.1088/0004-637X/764/2/184](https://doi.org/10.1088/0004-637X/764/2/184)
- McNamara, B. R., & Nulsen, P. E. J. 2007, ARA&A, 45, 117, doi: [10.1146/annurev.astro.45.051806.110625](https://doi.org/10.1146/annurev.astro.45.051806.110625)
- Merloni, A., & Heinz, S. 2008, MNRAS, 388, 1011, doi: [10.1111/j.1365-2966.2008.13472.x](https://doi.org/10.1111/j.1365-2966.2008.13472.x)

- Nawaz, M. A., Wagner, A. Y., Bicknell, G. V., Sutherland, R. S., & McNamara, B. R. 2014, *MNRAS*, 444, 1600, doi: [10.1093/mnras/stu1563](https://doi.org/10.1093/mnras/stu1563)
- Nesvadba, N. P. H., Lehnert, M. D., De Breuck, C., Gilbert, A. M., & van Breugel, W. 2008, *A&A*, 491, 407, doi: [10.1051/0004-6361:200810346](https://doi.org/10.1051/0004-6361:200810346)
- Novak, M., Smolčić, V., Schinnerer, E., et al. 2018, *A&A*, 614, A47, doi: [10.1051/0004-6361/201731635](https://doi.org/10.1051/0004-6361/201731635)
- Novak, M., Smolčić, V., Delhaize, J., et al. 2017, *A&A*, 602, A5, doi: [10.1051/0004-6361/201629436](https://doi.org/10.1051/0004-6361/201629436)
- Ocran, E. F., Taylor, A. R., Vaccari, M., et al. 2020, *MNRAS*, 500, 4685, doi: [10.1093/mnras/staa3538](https://doi.org/10.1093/mnras/staa3538)
- O'Sullivan, E., Giacintucci, S., David, L. P., et al. 2011, *ApJ*, 735, 11, doi: [10.1088/0004-637X/735/1/11](https://doi.org/10.1088/0004-637X/735/1/11)
- Padovani, P. 2016, *Astronomy and Astrophysics Review*, 24, 13, doi: [10.1007/s00159-016-0098-6](https://doi.org/10.1007/s00159-016-0098-6)
- Padovani, P., Bonzini, M., Kellermann, K. I., et al. 2015, *MNRAS*, 452, 1263, doi: [10.1093/mnras/stv1375](https://doi.org/10.1093/mnras/stv1375)
- Page, M. J., & Carrera, F. J. 2000, *MNRAS*, 311, 433, doi: [10.1046/j.1365-8711.2000.03105.x](https://doi.org/10.1046/j.1365-8711.2000.03105.x)
- Pei, Y. C. 1995, *ApJ*, 438, 623, doi: [10.1086/175105](https://doi.org/10.1086/175105)
- Pracy, M. B., Ching, J. H. Y., Sadler, E. M., et al. 2016, *MNRAS*, 460, 2, doi: [10.1093/mnras/stw910](https://doi.org/10.1093/mnras/stw910)
- Rafferty, D. A., McNamara, B. R., Nulsen, P. E. J., & Wise, M. W. 2006, *ApJ*, 652, 216, doi: [10.1086/507672](https://doi.org/10.1086/507672)
- Rigby, E. E., Argyle, J., Best, P. N., Rosario, D., & Röttgering, H. J. A. 2015, *A&A*, 581, A96, doi: [10.1051/0004-6361/201526475](https://doi.org/10.1051/0004-6361/201526475)
- Rigby, E. E., Best, P. N., Brookes, M. H., et al. 2011, *MNRAS*, 416, 1900, doi: [10.1111/j.1365-2966.2011.19167.x](https://doi.org/10.1111/j.1365-2966.2011.19167.x)
- Sani, E., Marconi, A., Hunt, L. K., & Risaliti, G. 2011, *MNRAS*, 413, 1479, doi: [10.1111/j.1365-2966.2011.18229.x](https://doi.org/10.1111/j.1365-2966.2011.18229.x)
- Saunders, W., Rowan-Robinson, M., Lawrence, A., et al. 1990, *Monthly Notices of the Royal Astronomical Society*, 242, 318
- Schaye, J., Crain, R. A., Bower, R. G., et al. 2015, *MNRAS*, 446, 521, doi: [10.1093/mnras/stu2058](https://doi.org/10.1093/mnras/stu2058)
- Schmidt, M. 1968, *ApJ*, 151, 393, doi: [10.1086/149446](https://doi.org/10.1086/149446)
- Schmidt, M., & Green, R. F. 1983, *Astrophys. J.*, 269, 352, doi: [10.1086/161048](https://doi.org/10.1086/161048)
- Schwarz, G. 1978, *The Annals of Statistics*, 6, 461, doi: [10.1214/aos/1176344136](https://doi.org/10.1214/aos/1176344136)
- Shankar, F., Cavaliere, A., Cirasuolo, M., & Maraschi, L. 2008, *ApJ*, 676, 131, doi: [10.1086/528836](https://doi.org/10.1086/528836)
- Singal, J., Ko, A., & Petrosian, V. 2014, *The Astrophysical Journal*, 786, 109
- Singal, J., Petrosian, V., Lawrence, A., et al. 2013, *The Astrophysical Journal*, 764, 43
- Smolčić, V., Novak, M., Delvecchio, I., et al. 2017a, *A&A*, 602, A6, doi: [10.1051/0004-6361/201730685](https://doi.org/10.1051/0004-6361/201730685)
- Smolčić, V., Novak, M., Bondi, M., et al. 2017b, *A&A*, 602, A1, doi: [10.1051/0004-6361/201628704](https://doi.org/10.1051/0004-6361/201628704)
- Smolčić, V., Zamorani, G., Schinnerer, E., et al. 2009, *ApJ*, 696, 24, doi: [10.1088/0004-637X/696/1/24](https://doi.org/10.1088/0004-637X/696/1/24)
- Smolčić, V., Delvecchio, I., Zamorani, G., et al. 2017, *A&A*, 602, A2, doi: [10.1051/0004-6361/201630223](https://doi.org/10.1051/0004-6361/201630223)
- Smolčić, V., Intema, H., Šlaus, B., et al. 2018, *A&A*, 620, A14, doi: [10.1051/0004-6361/201732336](https://doi.org/10.1051/0004-6361/201732336)
- Sołtan, A. 1982, *MNRAS*, 200, 115, doi: [10.1093/mnras/200.1.115](https://doi.org/10.1093/mnras/200.1.115)
- Springel, V., Pakmor, R., Pillepich, A., et al. 2018, *MNRAS*, 475, 676, doi: [10.1093/mnras/stx3304](https://doi.org/10.1093/mnras/stx3304)
- Takeuchi, T. T. 2000, *Astrophysics and Space Science*, 271, 213
- Tombesi, F., Meléndez, M., Veilleux, S., et al. 2015, *Nature*, 519, 436, doi: [10.1038/nature14261](https://doi.org/10.1038/nature14261)
- Tucci, M., & Toffolatti, L. 2021, *A&A*, 650, A127, doi: [10.1051/0004-6361/202039884](https://doi.org/10.1051/0004-6361/202039884)
- Ueda, Y., Akiyama, M., Ohta, K., & Miyaji, T. 2003, *ApJ*, 598, 886, doi: [10.1086/378940](https://doi.org/10.1086/378940)
- Urry, C. M., & Padovani, P. 1995, *PASP*, 107, 803, doi: [10.1086/133630](https://doi.org/10.1086/133630)
- van der Vlugt, D., Hodge, J. A., Algera, H. S. B., et al. 2022, *ApJ*, 941, 10, doi: [10.3847/1538-4357/ac99db](https://doi.org/10.3847/1538-4357/ac99db)
- Veilleux, S., Meléndez, M., Sturm, E., et al. 2013, *ApJ*, 776, 27, doi: [10.1088/0004-637X/776/1/27](https://doi.org/10.1088/0004-637X/776/1/27)
- Šlaus, B., Smolčić, V., Novak, M., et al. 2020, *A&A*, 638, A46, doi: [10.1051/0004-6361/201937258](https://doi.org/10.1051/0004-6361/201937258)
- Šlaus, B., Smolčić, V., Ivezić, Ž., et al. 2024, *A&A*, 684, A19, doi: [10.1051/0004-6361/202346947](https://doi.org/10.1051/0004-6361/202346947)
- Waddington, I., Dunlop, J. S., Peacock, J. A., & Windhorst, R. A. 2001, *MNRAS*, 328, 882, doi: [10.1046/j.1365-8711.2001.04934.x](https://doi.org/10.1046/j.1365-8711.2001.04934.x)
- Wall, J. V., & Peacock, J. A. 1985, *MNRAS*, 216, 173, doi: [10.1093/mnras/216.2.173](https://doi.org/10.1093/mnras/216.2.173)
- Wang, W., Yuan, Z., Yu, H., et al. 2026, *ApJ*, 997, 176, doi: [10.3847/1538-4357/ae2474](https://doi.org/10.3847/1538-4357/ae2474)
- Wang, W., Yuan, Z., Yu, H., & Mao, J. 2024, *A&A*, 683, A174, doi: [10.1051/0004-6361/202347746](https://doi.org/10.1051/0004-6361/202347746)
- Willott, C. J., Rawlings, S., Blundell, K. M., & Lacy, M. 1999, *MNRAS*, 309, 1017, doi: [10.1046/j.1365-8711.1999.02907.x](https://doi.org/10.1046/j.1365-8711.1999.02907.x)
- Willott, C. J., Rawlings, S., Blundell, K. M., Lacy, M., & Eales, S. A. 2001, *MNRAS*, 322, 536, doi: [10.1046/j.1365-8711.2001.04101.x](https://doi.org/10.1046/j.1365-8711.2001.04101.x)
- Yuan, Z., & Wang, J. 2013, *Ap&SS*, 345, 305, doi: [10.1007/s10509-013-1402-9](https://doi.org/10.1007/s10509-013-1402-9)

Yuan, Z., Wang, J., Zhou, M., & Mao, J. 2016a, ApJ, 829,
95, doi: [10.3847/0004-637X/829/2/95](https://doi.org/10.3847/0004-637X/829/2/95)
—. 2016b, ApJ, 820, 65, doi: [10.3847/0004-637X/820/1/65](https://doi.org/10.3847/0004-637X/820/1/65)

Yuan, Z., Wang, J., Zhou, M., Qin, L., & Mao, J. 2017, The
Astrophysical Journal, 846, 78

APPENDIX

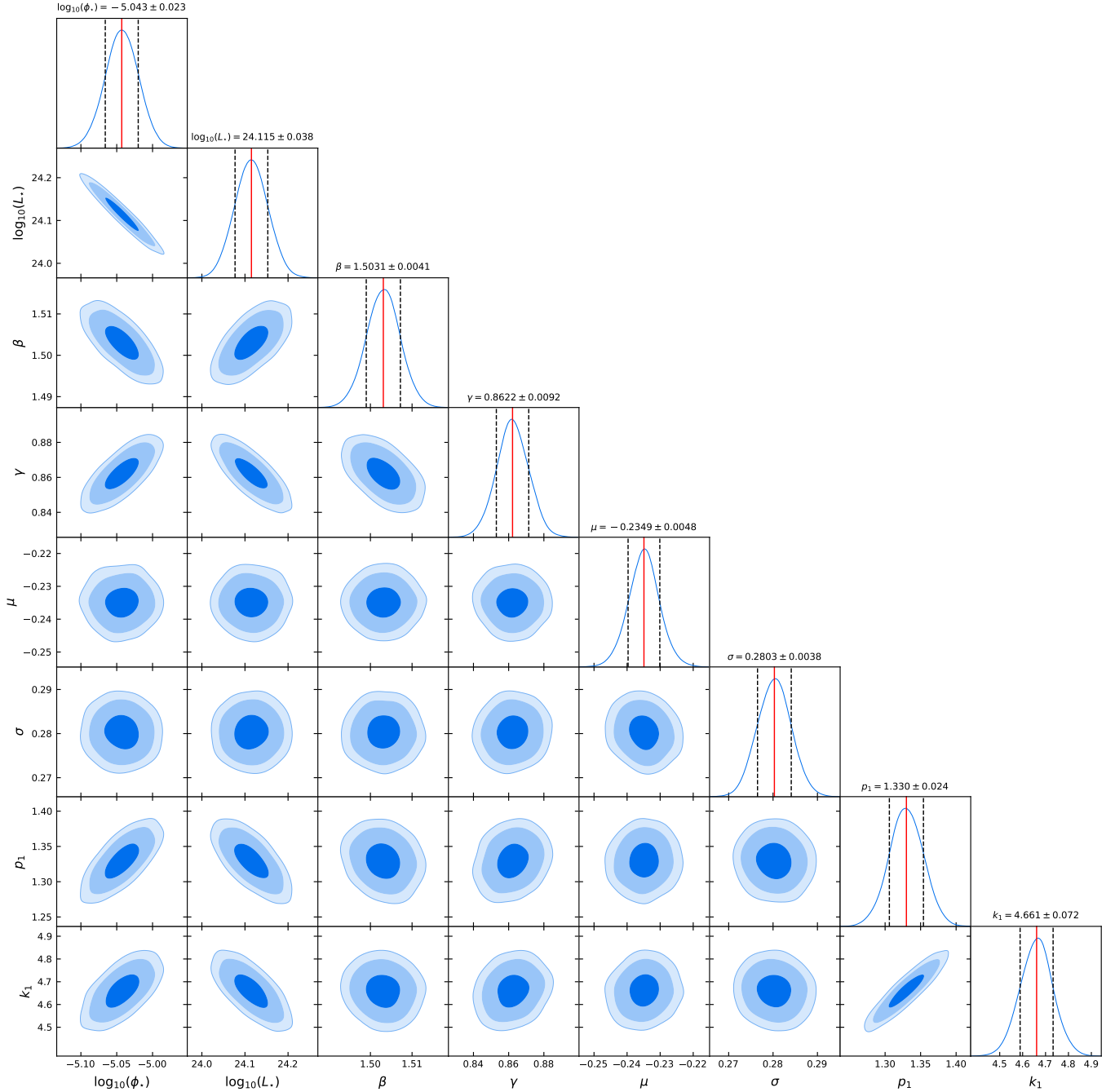


Figure 12. Corner plot illustrating the one- and two-dimensional projections of the posterior probability distributions for Model A, derived from the MCMC sampling. The diagonal panels display the marginalized posterior distributions for each parameter, with the 16th and 84th percentiles indicated by vertical dashed lines. The off-diagonal panels present the two-dimensional joint posterior distributions for each parameter pair, with 1 σ , 2 σ , and 3 σ confidence levels indicated by blue regions of varying depth. The red vertical solid lines indicate the best-fitting parameter values.

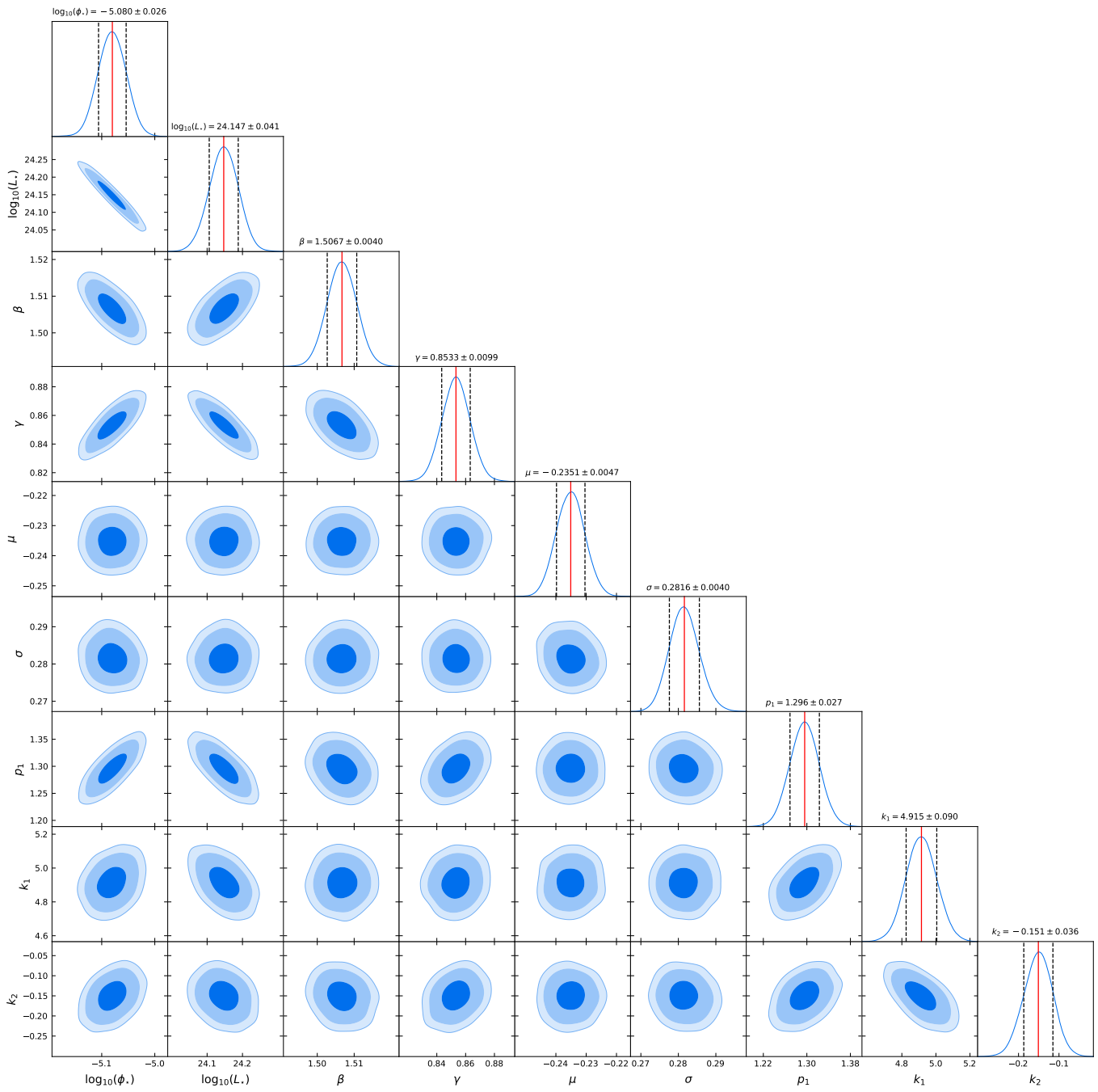


Figure 13. Similar to Figure 12, but for Model B.

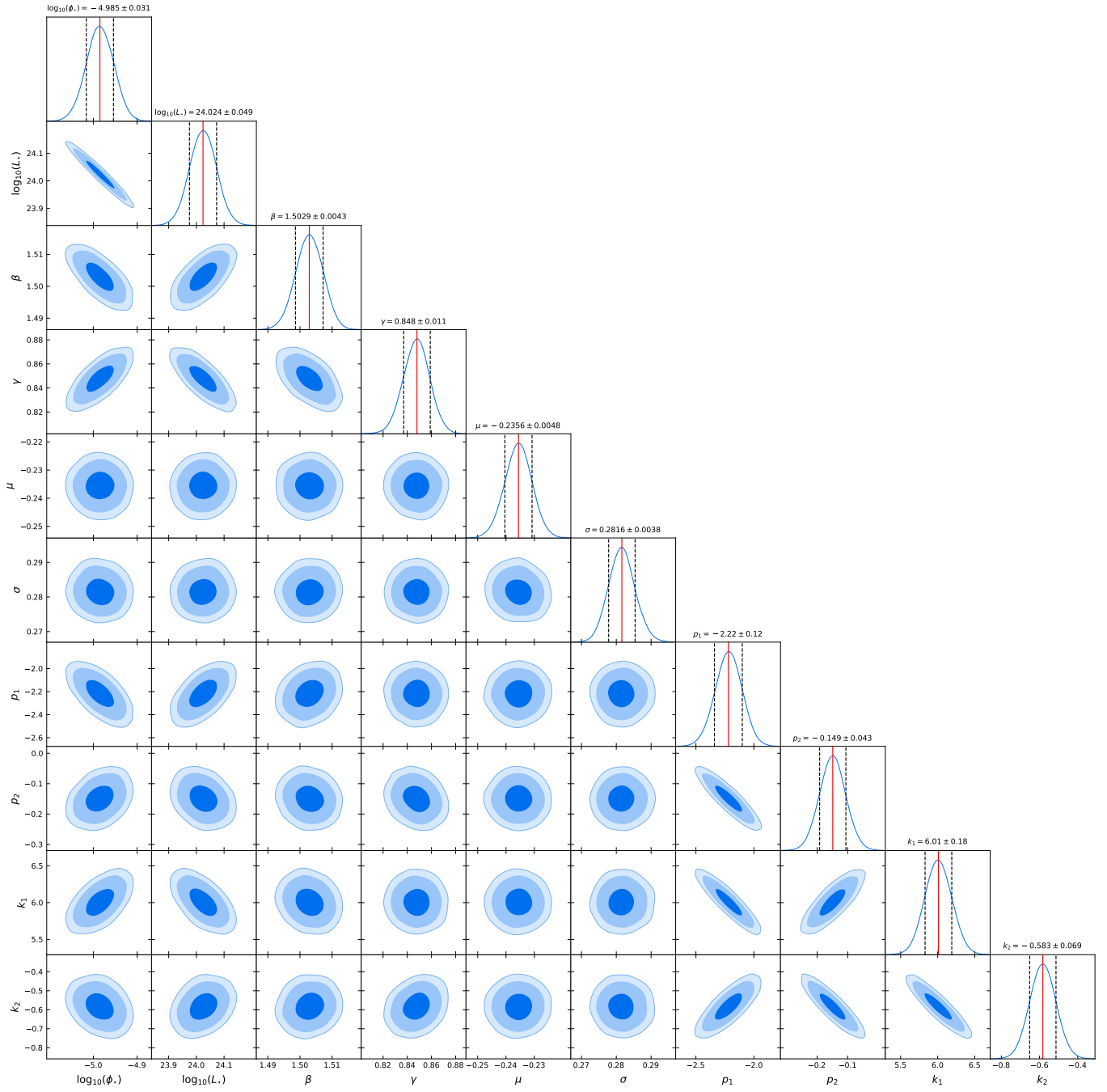


Figure 14. Similar to Figure 12, but for Model C.